TAMPERE UNIVERSITY OF TECHNOLOGY
Department of Electrical Engineering

JYRI KIVIMÄKI
DESIGN ISSUES IN IMPLEMENTING MAXIMUM-POWER-POINT TRACKING ALGORITHMS FOR PV APPLICATIONS

Master of Science Thesis

Examiner: Teuvo Suntio
The examiner and the topic were approved in the Faculty of Computing and Electrical Engineering Council meeting on 13.8.2014

TIIVISTELMÄ

TAMPEREEN TEKNILLINEN YLIOPISTO
Sähkötekniikan diplomi-insinöörin tutkinto
KIVIMÄKI, JYRI: Design Issues in Implementing Maximum-Power-Point Tracking Algorithms for PV Applications
Diplomityö, 62 sivua, 5 liitesivua
Maaliskuu 2015
Pääaine: Sähkökäyttöjen tehoelektroniikka
Tarkastaja: Prof. Teuvo Suntio
Avainsanat: aurinkosähkö, maksimitehopisteen seuranta, poikkeuttavat algoritmit, optimointi

Aurinkosähkögeneraattorilla on epälineaarinen virta-jännite riippuvuus, jonka vuoksi sillä on erityinen maksimitehopiste, jossa generaattorin teho on suurimmillaan. Koska maksimitehopiste riippuu säteilytehointensiteetin voimakkuudesta ja lämpötilasta, täytyy generaattoriin kytketyssä tehoelektronisessa muuttajassa hyödyntää jonkinlaista maksimitehopisteen seurantaa (Maximum power point tracking, MPPT). Tämän työn tavoitteena oli tarjota suunnitteluohjeet, jolla saavutetaan hyvä MPPT-suorituskyky mahdollisimman yksinkertaisella algoritmilla. Viimeisten vuosikymmenten aikana on kehitetty useita MPPT-algoritmeja. Tässä diplomityössä keskityttiin kuitenkin tavallisten poikkeuttavien (perturbative) MPPT-tekniikoiden sekä niihin kehitettyjen parannusten toimintaan muuttuvissa ja muuttumattomissa olosuhteissa.

Tavallisten poikkeuttavien MPPT-tekniikoiden heikkous on se, että niissä täytyy valita joko pieni jatkuvan tilan värähtely tai nopea muutostilanteiden vaste. Sen vuoksi suunnitteluparametrit, poikkeuttamisaskeleen koko ja päivitysnopeus, täytyy optimoida, jotta suurin mahdollinen MPPT-hyötysuhde saavutetaan. Päivitysnopeus täytyy valita mahdollisimman lyhyeksi, jotta algoritmi toimii oikein nopeissa säteilytehointensiteetin muutostilanteissa. Maksiminopeuden määrittää teholähteen tulopuolen dynamiikka, koska tehon värähtely muutostilanteen jälkeen täytyy olla asettunut jatkuvan tilan arvoonsa ennen uuden poikkeuttamisen suorittamista. Toisaalta poikkeuttamisaskel täytyy valita siten, että poikkeuttamisesta aiheutuva tehon muutos on suurempi kuin mikä tahansa muu tekijä, joka voi aiheuttaa muutoksen generaattorin tehossa.

Simulointien perusteella perinteisillä poikkeuttavilla MPPT-menetelmillä voidaan saavuttaa korkea pysyvän ja muuttuvan tilan hyötysuhde, kun suunnitteluparametrit on valittu optimaalisesti. Vastaavasti mittauksista kävi ilmi, että erilaisilla epävarmuustekijöillä (uncertainty) mittauspiirissä on suuri vaikutus poikkeuttavien algoritmien hyötysuhteeseen. Suurimmat epävarmuustekijät liittyvät mittaussignaalien kohinaan ja analogia-digitaalimuuntimien resoluutioon. Sen vuoksi suunniteltaessa poikkeuttavaa maksimitehopisteen seurantajärjestelmää, täytyy kiinnittää huomioita pääasiallisiin kohinan lähteisiin, jotka voivat vaikuttaa MPPT-algoritmin toimintaan.

ABSTRACT

TAMPERE UNIVERSITY OF TECHNOLOGY
Master's Degree Programme in Electrical Engineering
JYRI KIVIMÄKI: Design Issues in Implementing Maximum-Power-Point Tracking Algorithms for PV Applications
Master of Science Thesis, 62 pages, 5 Appendix pages
March 2015
Major: Power Electronics of Electrical Drives
Examiner: Prof: Teuvo Suntio
Keywords: photovoltaic, maximum power point tracking, perturbative algorithms, optimization

A photovoltaic generator (PVG) has a nonlinear current-voltage characteristic with a special maximum power point (MPP), which depends on the environmental factors such as temperature and irradiation. In order to obtain maximum amount of energy from PVG, the power electronic converter connected to the PVG need to utilize some sort of technique for maximum power point tracking (MPPT). The aim of the thesis was to study different MPPT techniques to find the design rules, which offer the balance between the complexity and speed of the MPPT algorithm. Despite a significant amount of developed MPPT algorithms, perturbative MPPT algorithms and their corresponding improved versions were analyzed more thoroughly in this thesis due to the fact that they have been shown to provide good balance between complexity and MPPT performance. These algorithms were tested in steady-state and dynamic conditions.

The conventional perturbative MPPT algorithms have a drawback of trade-off between steady-state oscillations and fast dynamics. Therefore, the design variables the perturbation step size and the sampling frequency need to be optimized carefully to ensure proper operation yielding the highest possible efficiency. Sampling frequency of the perturbative algorithm should be selected as fast as possible to obtain the fastest dynamics in varying atmospheric conditions. However, the sampling frequency should not be selected faster than the PVG power settling time to guarantee that oscillatory behavior do not affect the decision process of perturbation sign. In contrast, the perturbation step-size has a significant effect on steady-state MPPT efficiency and on performance in dynamic atmospheric condition. To ensure proper operation in all atmospheric conditions, the power change in PVG caused by perturbation needs to be larger than the power change caused by any other external source such as irradiance variation, output voltage fluctuation and uncertainty factors in the measurement circuit.

Based on the simulations, high MPPT efficiency can be achieved even with conventional perturbative algorithms if these are properly optimized. Moreover, the experimental measurements have shown that the uncertainty factors such as noise and quantization errors in the measurement circuit play a significant role in the operation of perturbative algorithm. Therefore, the minimization of uncertainty must be focused on the noise sources that would influence most the decision process of the MPPT.

PREFACE

This Master of Science thesis was done for the Department of Electrical Engineering at Tampere University of Technology. The examiner of the thesis was Prof. Teuvo Suntio.

Also I want to thank Prof. Teuvo Suntio for interesting topic and guidance during the whole process. Finally, I want to thank all the team involved in my thesis work, Ph.D. Tuomas Messo, M.Sc. Juha Jokipii, M.Sc. Jukka Viinamäki, M.Sc. Aapo Aapro, B.Sc. Matti Marjanen and B.Sc. Julius Schnabel for inspiring and great working environment.

Tampere 1.3.2015

Jyri Kivimäki

CONTENTS

TERMS AND SYMBOLS

GREEK CHARACTERS

Δ	Characteristic polynomial
ϵ	Relative magnitude
η_{eu}	European efficiency in steady-state condition
η_{mppt}	Maximum power point tracking efficiency
ω_{n}	Converter natural angular frequency
ω_{p}	Input voltage controller pole angular frequency
ω_{s}	Grid fundamental angular frequency
ω_{z}	Input voltage controller zero angular frequency
ζ	Damping factor

LATIN CHARACTERS

$\mathbf{A}$	System matrix
a	Diode ideality factor
$\mathbf{B}$	Input matrix
B	Maximum bits in an analog-to-digital converter
$\mathbf{C}$	Output matrix
C	Capacitance
d	Duty ratio
d'	Complement of the duty ratio
Δd	Increment in the duty ratio
Δd_{max}	Maximum increment in the duty ratio
$\mathbf{D}$	Input-output matrix
D	Steady-state value of duty ratio
$\mathbf{G}$	Matrix containing transfer functions of a converter
G	Irradiance
$\dot{G}$	Rate of change of irradiance
G_{a}	Gain of the pulse width modulator
G_{c}	Voltage controller transfer function
$G_{\mathrm{ci-c}}$	Closed-loop control-to-input transfer function
$G_{\mathrm{ci-o}}$	Open-loop control-to-input transfer function
$G_{\mathrm{ci-o}}^{\mathrm{S}}$	Source-affected open-loop control-to-input transfer function
$G_{\mathrm{co-o}}$	Open-loop control-to-output transfer function
$G_{\mathrm{co-o}}^{\mathrm{S}}$	Source-affected open-loop control-to-output transfer function
G_{ri}	Reference-to-input transfer function
$G_{\mathrm{io-c}}$	Closed-loop input-to-output transfer function
$G_{\mathrm{io-o}}$	Open-loop input-to-output transfer function
$G_{\mathrm{io-o}}^{\mathrm{S}}$	Source-affected input-to-output transfer function
$G_{\mathrm{io-\infty}}$	Ideal input-to-output transfer function
$G_{\mathrm{io-o}}^{\mathrm{S}}$	Source-affected open-loop input-to-output transfer function
$G_{\mathrm{se-i}}^{\mathrm{in}}$	Input current sensing gain
$G_{\mathrm{se-u}}^{\mathrm{in}}$	Input voltage sensing gain
$\mathbf{I}$	Identity matrix
H	Auxiliary variable
I_{mpp}	Current of the maximum power point
$I_{\mathrm{mpp,stc}}$	Current of the maximum power point in standard test condition

I_pv	Steady-state current of a photovoltaic generator
ΔI_G	Incremental change in current due to variation in irradiance
ΔI_x	Incremental change in current due to perturbation step
ΔI_pv	Incremental change in the terminal current of a photovoltaic generator
i_d	Diode current
i_in	Input current of the converter
$i_\mathrm{se,in}$	Sensed input current
i_o	Output current of the converter
i_L	Inductor current
i_pv	Terminal current of a photovoltaic generator
$i_\mathrm{sc,stc}$	Short-circuit current in standard test condition
k	Boltzmann constant or time instant
K_in	Input voltage controller gain
K_i	Temperature coefficient of short-circuit current
K_ph	Material constant
L	Inductance
L_in	Input voltage control loop
N	Scaling factor
N_s	Number of series connected cells in photovoltaic module
P_pv	Average output power of a photovoltaic generator
ΔP_G	Power change in a photovoltaic generator due to irradiance variation
ΔP_pv	Incremental change in the terminal power of a photovoltaic generator
ΔP_x	Power change in a photovoltaic generator due to perturbation step
q	Elementary charge
R_mpp	Static resistance of a photovoltaic generator at maximum power point
R_pv	Static resistance of a photovoltaic generator
r_C	Equivalent resistance of an capacitor
r_d	Forward resistance of a diode
r_L	Equivalent resistance of an inductor
r_pv	Dynamic resistance of a photovoltaic generator
r_s	Parasitic series resistance of a photovoltaic cell
r_sh	Parasitic shunt resistance of a photovoltaic cell
s	Laplace variable
T	Temperature
T_s	Switching period
$T_\mathrm{oi-c}$	Closed-loop reverse voltage transfer function
$T_\mathrm{oi-o}$	Open-loop reverse voltage transfer function
$T_\mathrm{oi-o}^\mathrm{S}$	Source-affected open-loop reverse voltage transfer function
$T_{\mathrm{oi}-\infty}$	Ideal output-to-input transfer function
T_p	Sampling period of a maximum power point tracking algorithm
T_ϵ	Power settling time of a photovoltaic generator
$\mathbf{U}$	Vector containing Laplace transformed input variables
U_mpp	Voltage of the maximum power point
$U_\mathrm{mpp,stc}$	Voltage of the maximum power point in standard test condition
U_pv	Steady-state voltage of a photovoltaic generator
U_fs	Full-scale voltage in analog-to-digital converter
ΔU_o	Amplitude of output voltage fluctuation
ΔU_pv	Incremental change in the terminal voltage of a photovoltaic generator
ΔU_x	Incremental change in voltage due to perturbation step

$u_{\mathrm{oc,stc}}$	Open-circuit voltage in standard test condition
u_{pv}	Terminal voltage of a photovoltaic generator
$u_{\mathrm{se,in}}$	Sensed input voltage
$\mathbf{u}_{\mathrm{i}}$	Current uncertainty
$\mathbf{u}_{\mathrm{u}}$	Voltage uncertainty
$\mathbf{u}_{\mathrm{p}}$	Power uncertainty
$\Delta u^{\mathrm{in}}_{\mathrm{ref}}$	Incremental change in input voltage reference
$\hat{x}$	AC-perturbation around a steady-state operation point
$\langle x \rangle$	Average value of variable x
Δx	Incremental change in a perturbed variable
$\mathbf{Y}$	Vector containing Laplace transformed output variables
$Y_{\mathrm{o-sci}}$	Short-circuit output admittance
$Y_{\mathrm{o}-\infty}$	Ideal output admittance
Y_{S}	Output admittance of a non-ideal source
$Z_{\mathrm{in-c}}$	Closed-loop input impedance
$Z_{\mathrm{in-oco}}$	Open circuit input impedance
$Z_{\mathrm{in}-\infty}$	Ideal input impedance
$Z_{\mathrm{in-o}}$	Open-loop input impedance
$Z^{\mathrm{S}}_{\mathrm{in-o}}$	Source-affected open-loop control-to-output transfer function

ABBREVIATIONS

AC	Alternating current
ADC	Analog-to-digital converter
CC	Constant current
CCM	Continous conduction mode
CF	Current-fed
CV	Constant voltage
DC	Direct current
DCM	Discontinous conduction mode
ES	Extrenum seeking
GM	Gain margin
IC	Incremental Conductance
KCL	Kirchoff current law
KVL	Kirchoff voltage law
LSB	Least significant bit
MPP	Maximum power point
MPPT	Maximum power point tracking
OC	Open-circuit
PID	Proportional integral derivative
PM	Phase margin
PSO	Particle Swarm Optimization
PV	Photovoltaic
PWM	Pulse width modulation
P&O	Perturb and Observe
dP-P&O	Perturb and Observe with additional power sample
RCC	Ripple correlation control
SC	Short-circuit
SF	Sizing factor
STC	Standard test conditions

1. INTRODUCTION

Modern society has become more and more dependent on energy. Growing energy demand and concern about global warming due to fossil fuels has driven researchers to further develop renewable energy resources such as hydro, geothermal, biofuel, wind and solar. Despite the fact that oil will run out in this century, approximately 87 % of total produced energy is still generated by fossil fuels. Therefore, it is obvious that research in the field of renewable energy resource must be increased. Solar energy is one of the most promising renewable energy sources, because it is free, clean and abundantly available. [1]

A photovoltaic generator (PVG) has a nonlinear current-voltage characteristic, with a distinct maximum power point (MPP), which depends on the environmental factors, such as temperature and irradiation. In order to extract maximum power from a PVG, they have to operate at their MPP despite the unpredictable changes in atmospheric conditions. Therefore, the controllers of all solar power electronic converters employ some method for maximum power point tracking (MPPT). Over the past decades, several MPPT techniques have been published varying in complexity, sensors required, cost, convergence speed, range of effectiveness and implementation hardware. [2]

The aim of this thesis is to study different MPPT techniques to find the design rules, which offer the balance between the complexity and speed of the MPPT algorithm. To be more precise, it would be valuable to find out what are the requirements for MPPT to achieve over 99.5 % efficiency in steady-state and fast-changing irradiance conditions. In this thesis, perturbative MPPT algorithms were analyzed more thoroughly due to the fact that they have shown to offer good performance in different atmospheric conditions in spite of a simple implementation.

The rest of the thesis is organized as follows: In the second chapter, the characteristics of the PV cell is introduced. Chapter 3 introduces the properties of a boost-power-stage converter in PV application including its dynamic analysis. Chapter 4 focuses on MPPT algorithms, including a brief overview of the most widely used MPPT algorithms. The rest of the Chapter 4 gives more detailed discussion on the conventional perturbative MPPT algorithms and their improved versions. Chapter 5 presents the measurements of the prototype converter. Chapter 6 finalizes the thesis by concluding the main points of the previous chapters.

2. PROPERTIES OF A PHOTOVOLTAIC MODULE

2.1 Modeling of a Photovoltaic Module

Due to the internal semiconductor junction, all the PV cells have essentially similar electrical performance. Therefore, it is possible to build a general model for single PV cell by using fundamental electrical components. Changing the parameters of these components, different cell types can be modeled. Several PV cell models have been introduced in literature and they differ in complexity and implementation purposes. However, a single-diode model is commonly used to model the electrical characteristics of PV cell due to good compromise between accuracy and complexity. A simplified electrical equivalent circuit of a PV cell composes of a photocurrent source with parallel-connected diode and parasitic elements as can be seen in Fig. 2.1, where a non-ideal diode represents the internal semiconductor junction and parasitic resistances correspond to the power losses.

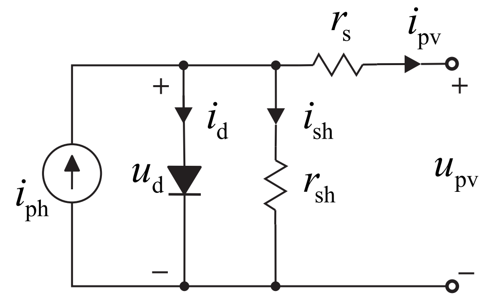

Figure 2.1: One diode model of a PV cell.

In Fig. 2.1, photovoltaic current i_{ph} describes the fundamental source of the produced current, i_{d} is the diode current, u_{d} is the diode voltage, i_{sh} is the current through the shunt resistance, i_{pv} is the output current of the cell and u_{pv} is the terminal voltage of the PV cell. [3]

PV cells are needed to be connected in series and/or parallel for electrical energy production purposes. This is due to the fact that an individual PV cell has low maximum voltage and power. In series connection, each PV cell increases the maximum voltage and parallel connection increases the maximum current of the system. By using both series and parallel connection, the required voltage and power levels can be achieved for the PV generator (PVG). [4]

The current-voltage (I-U) characteristic of the practical PV module, where several

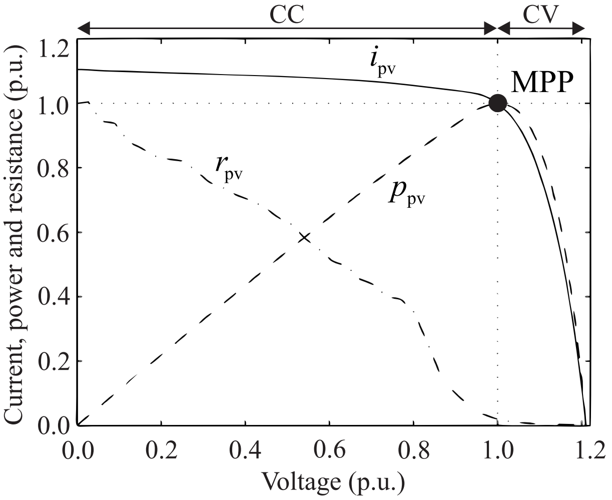

Figure 2.2: Typical I-U curve and dynamical resistance of a PV module relative to the MPP values.

cells are connected in series, can be presented according to following equation [3]:

$$i_{\mathrm{pv}} = i_{\mathrm{ph}} - \underbrace{i_0 \left[\exp\left(\frac{u_{\mathrm{pv}} + r_{\mathrm{s}} i_{\mathrm{pv}}}{N_{\mathrm{s}} a k T / q}\right) - 1\right]}_{i_{\mathrm{d}}} - \underbrace{\frac{u_{\mathrm{pv}} + r_{\mathrm{s}} i_{\mathrm{pv}}}{r_{\mathrm{sh}}}}_{i_{\mathrm{sh}}}, \tag{2.1}$$

where i_0 is diode saturation current, N_{s} the number of cells connected in series, a the diode ideality factor, k the Bolzmann coefficient and q the elementary charge. The second and third term in (2.1) represent current through the diode and shunt resistance, respectively. Based on (2.1), the I-U curve of a PV panel can be depicted as shown in Fig. 2.2 revealing the special characteristics of the source. The dynamic resistance r_{pv} includes the effect of the diode, series resistance and shunt resistance. As can be concluded from Fig. 2.2, the dynamic resistance is non-linear and operation-point dependent and it is defined as the slope $\Delta u_{\mathrm{pv}}/\Delta i_{\mathrm{pv}}$ of an I-U curve. [5]

A PV cell has three special operation points: The short-circuit (SC) condition occurs when u_{pv} is zero and short-circuit current I_{sc} flows through PV cell. The second is open-circuit (OC) condition, where all the light generated current i_{ph} flows through the diode and current of PV cell is zero. This open-circuit voltage u_{oc} at PV cell terminals can be written as

$$u_{\mathrm{oc}} = \frac{akT}{q} \ln\left(1 + \frac{i_{\mathrm{sc}}}{i_0}\right). \tag{2.2}$$

The third important operation point is the maximum power point (MPP), where the current value is I_{mpp} and the voltage value is U_{mpp} yielding maximum power $P_{\mathrm{mpp}} = U_{\mathrm{mpp}} I_{\mathrm{mpp}}$ of a PV cell. All other operation points lie between these three points. Moreover, the MPP divides I-U curve into two operating regions. At the voltages lower than the MPP the region is called constant current (CC) region, where current stays relatively constant despite changes in voltage. Other side of MPP, at higher voltages, is called constant voltage (CV) region due to fact that current stays relatively constant while PVG voltage is limited due to forward biasing of the diode. In order to maximize the output power of the PVG, its operation point should be kept at MPP. At MPP, the derivative of PVG output power p_{pv} is zero, which can be represented by (2.3).

$$\frac{dp_{\mathrm{pv}}}{du_{\mathrm{pv}}} = \frac{d(u_{\mathrm{pv}} i_{\mathrm{pv}})}{du_{\mathrm{pv}}} = U_{\mathrm{pv}} + I_{\mathrm{pv}} \frac{\Delta u_{\mathrm{pv}}}{\Delta i_{\mathrm{pv}}} = 0 \Leftrightarrow \frac{U_{\mathrm{pv}}}{I_{\mathrm{pv}}} = -\frac{\Delta u_{\mathrm{pv}}}{\Delta i_{\mathrm{pv}}}, \tag{2.3}$$

where U_{pv} and I_{pv} are the PVG steady-state voltage and current, respectively. At the MPP, PV cell static resistance $R_{\mathrm{pv}} = U_{\mathrm{pv}}/I_{\mathrm{pv}}$ equals the dynamic resistance r_{pv}, i.e., at MPP following holds $r_{\mathrm{pv}} = R_{\mathrm{pv}} = R_{\mathrm{mpp}} = U_{\mathrm{mpp}}/I_{\mathrm{mpp}}$.

The PV panel manufacturers usually provide only the electrical parameters I_{sc}, U_{oc}, I_{mpp} and U_{mpp} of the PV panel. The values are given in specific operation conditions called standard test conditions (STC), where cell temperature is $25\,^{\circ}\mathrm{C}$, irradiance level is $1000\,\mathrm{W/m^2}$, and the value of air mass AM is 1.5. Basically, air mass means the mass of air between the PV module and the sun, which affects the spectral distribution and intensity of sunlight.

The accuracy of (2.1) can be further improved by including the effect of the ambient temperature on photocurrent. The photocurrent i_{ph} is linearly depedent on the solar irradiation and is also affected by ambient temperature as following

$$i_{\mathrm{ph}} = i_{\mathrm{ph,stc}} + K_{\mathrm{i}} \Delta_{\mathrm{T}} \frac{G}{G_{\mathrm{stc}}}, \tag{2.4}$$

where $i_{\mathrm{ph,stc}}$ is the photocurrent at the STC, K_{i} is the temperature coefficient, Δ_{T} is the difference between actual temperature and the temperature in STC, G is the actual irradiance on the surface of the PV module and G_{stc} refers to irradiance in STC.

The saturation current i_0 depends on the intrinsic characteristics and temperature of the PV cell and it can be calculated as the function of temperature by using (2.5).

$$i_0 = i_{0,\mathrm{stc}} \left(\frac{T_{\mathrm{stc}}}{T}\right)^3 \exp\left[\frac{qE_{\mathrm{g}}}{ak}\left(\frac{1}{T_{\mathrm{stc}}} - \frac{1}{T}\right)\right] \tag{2.5}$$

where T_{stc} is the temperature of the p-n junction in STC, T is actual temperature and E_{g} is the bandgap energy of the semiconductor. The nominal saturation current $i_{0,\mathrm{stc}}$ is linearly dependent on nominal short-circuit current $i_{\mathrm{sc,stc}}$ and logarithmically depedent on nominal open-circuit voltage $u_{\mathrm{oc,stc}}$ as follows

$$i_{0,\mathrm{stc}} = \frac{i_{\mathrm{sc,stc}}}{\exp\left(u_{\mathrm{oc,stc}} q / N_{\mathrm{s}} a k T_{\mathrm{stc}}\right) - 1} \tag{2.6}$$

In this thesis, NAPS NP190GKg PV Module is used as a PV source. The module is composed of 54 series-connected multicrystalline Si PV cells that are divided into three substrings of 18 cells protected by a bypass diode. The electrical characteristic of the PV module can be seen in Table 2.1, where the left column corresponds to the values reported in the manufacturer's datasheet.

Table 2.1: Electrical characteristic and parameters used in simulations for a NAPS NP190Gkg PV module in STC.

Parameter	Value	Parameter	Value
$U_{\mathrm{oc,stc}}$	33.1 V	K_{i}	0.0047 A/K
$I_{\mathrm{sc,stc}}$	8.02 A	R_{s}	0.33 Ω
$U_{\mathrm{mpp,stc}}$	25.9 V	R_{sh}	188 Ω
$I_{\mathrm{mpp,stc}}$	7.33	a	1.3
$P_{\mathrm{mpp,stc}}$	190 W		
N_{s}	54		

Since the datasheet provide only limited data from PV panel, the parameters in (2.1) need to calculated by using models. By using the introduced equations, a simulation model for NAPS190GKg PV module was developed, which was already verified in the prior research to be accurate [6].

2.2 Effect of Atmospheric Conditions

Photovoltaic cells are highly affected by operating conditions. These are mainly the value of irradiance on a PV cell and temperature of the p-n junction [3]. In Fig. 2.3, two power-voltage (P-U) curves were plotted based on (2.1) with different irradiance and temperature levels. As can be seen in Fig. 2.3b, temperature on a PV cell has a significant effect on open-circuit voltage affecting also MPP voltage value. On the contrary, it has a negligible effect on the value of short-circuit current. However, temperature on the PV cell is changing slowly with respect to variation of the irradiance level during the day and therefore, it is assumed to be constant in the calculations.

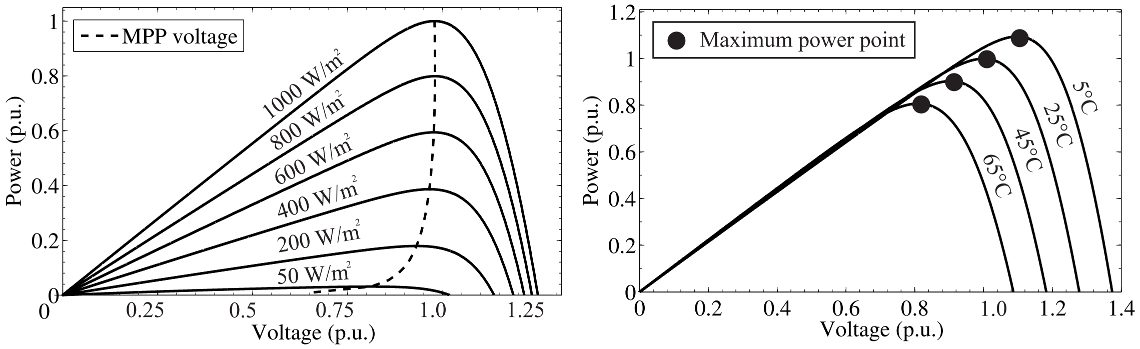

(a) (b)

Figure 2.3: Effect of irradiance variation (a) and temperature variation (b) relatively to MPP conditions in STC.

The irradiance variation is considered as the main issue from PVG energy production point of view. Since the photocurrent is directly proportional to the irradiance,

irradiance can change the operation point of the PVG to vary quickly due its unpredictability of wide and fast variation. The irradiance varies usually between 50–1000 W/m^2 during the day, whereas it can be up to 1500 W/m^2 with the duration of 20 s to 140 s under cloud enhancement condition [7]. In contrast, the speed of irradiance transitions can be up to several hundreds of W/m^2 in a second, whereas the average is approximately 30 W/m^{2}s depending on location. Distribution of maximum rate of change of irradiance transitions in [8] is depicted in the Fig. 2.4 recorded from Tampere University of Technology Solar Photovoltaic Power Station Research Plant.

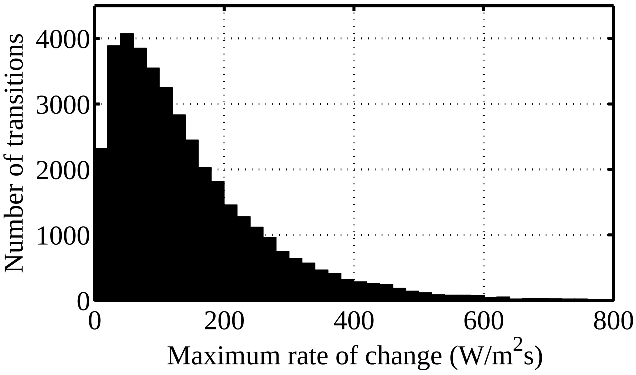

Figure 2.4: Distribution of maximum rate of change of irradiance transitions.

In the figure, all the discussed transitions in [8] are collected in the same picture, which are recorded during 50 days. It can be seen that slower irradiance slopes appear most frequently, where the most frequently existing rate of change of irradiance transitions are $20 - 80$ W/m^2. However, a noticeable amount of transitions with the rate of change up to 600 W/m^2 does exit.

Since the photocurrent is directly proportional to the irradiance, it can be noticed that irradiance can change the operation point of the PVG to vary quickly. However, the MPP voltage variation in respect to the irradiance is negligible in mid-to-high irradiance levels as can be concluded in Fig. 2.3a. In contrast, MPP voltage strongly decreases in low irradiance levels, which is due to the fact that open-circuit voltage is logarithmically dependent on irradiance, thus, the effect is most significant at low irradiance levels. Nevertheless, by looking Fig. 2.3 at low irradiance levels (i.e. $0 - 100$ W/m^2), the curve around the MPP is more flat and therefore, the voltage variation is usually neglected [3].

2.3 Partial Shading

Available voltage and power from a single PV cell is low and therefore, multiple cells must be connected in series or/and parallel for electrial energy production purposes. In long series-connected PV cells, however, a single or several cells can be exposed to different irradiance levels causing mismatch power losses. The phenomenon is called partial shading, which can occur due to several reasons such as buildings, clouds or trees. In case of partial shading condition, if one PV cell of the generator composed of series-connected cells is shaded, the SC currents of the non-shaded cells are higher than the DC current of the shaded cells. Shaded cell becomes reverse-biased due to other cells connected in series and the maximum energy yield is reduced compared to the uniform irradiance condition.

Partial shading of a PV generator can cause multiple MPPs to appear in the generator. That compromises the energy yield when the generator is operating at a local MPP instead of global MPP. [6] The number of the local maxima in power-voltage curve is defined by the configuration of bypass-diodes. The bypass-diodes are needed to connected antiparallel with the PV cells to prevent hot spot heating during the partial shading. The bypass diode limits the negative voltage of a cell group to its threshold voltage enabling current to flow. Fig. 2.5 represents the condition, where one third of a PV module with three bypass diodes is shaded with different shading intensities.

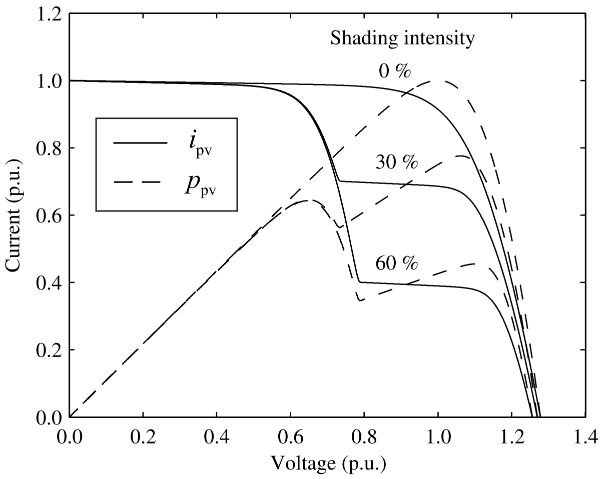

Figure 2.5: PVG characteristic in partial shading condition.

In low shading intensities, global MPP is found at higher voltages, whereas high shading intensity causes global MPP to be found at lower voltages. Although, the partial shading phenomenon will not be deeply discussed in this thesis, a brief overview of different global MPPT techniques is given in Chapter 4.

3. OPERATION OF A BOOST-POWER-STAGE CONVERTER

In conventional PV systems, produced energy is fed to a battery and used locally. Nowadays, it is more common to feed the energy into the electricity grid. In grid-connected PV systems, the final stage in the power conversion chain is the grid-connected inverter, which enables power transfer from a DC source into an AC load. Different configurations can be used to implement the DC-AC conversion, which are typically divided into four different configurations: module-integrated, string, central, and multistring inverter as depicted in Fig. 3.1. [9] The DC-AC conversion can be implemented either with one or two-stage conversion scheme. In one-stage scheme, PVG is directly connected to the input of inverter, which feeds the AC voltages and currents to the grid. However, due to the inherent step-down characteristics of the inverter bridge, a single-stage inverter requires that the PVG voltage is higher than the peak AC voltage value. Therefore, PV modules need to be connected into large strings, which are more sensitive to the partial shading conditions [6]. It is neither suitable for low-power PV applications such as microinverters.

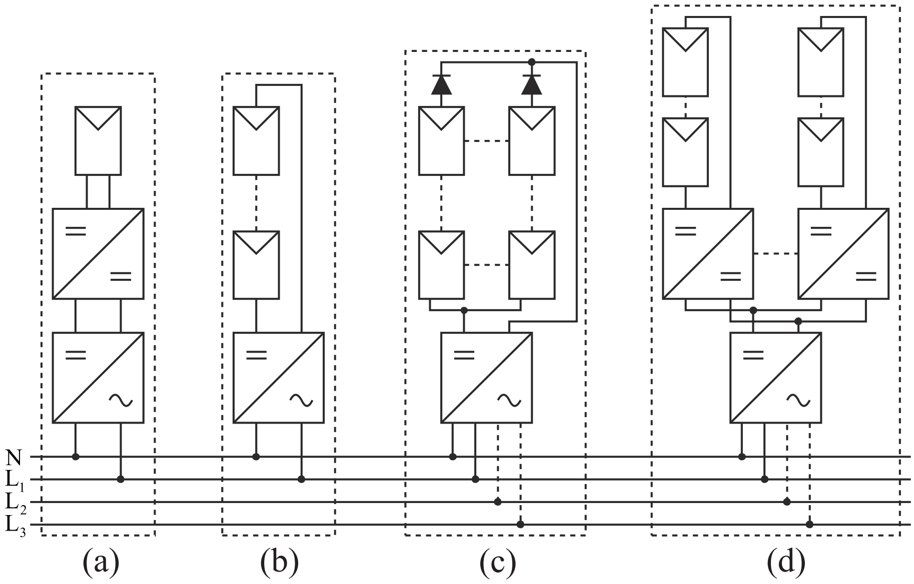

Figure 3.1: Different inverter concepts used in PV power systems are (a) module-integrated (b) string (c) central (d) multistring inverter. [9]

The two-stage scheme is based on a DC-DC converter that controls PVG voltage via MPPT algorithm, which is depicted in Fig. 3.2. Voltage-boosting DC-DC converter enables that less series-connected photovoltaic cells and modules are needed and wider voltage range can be used. Moreover, an additional blocking diode is not needed to prevent current flowing back to the PVG during low irradiation as it is already included in the boost-power-stage [10]. It has been also shown that in case of two-stage inverter, input-voltage control of the DC-DC converter transforms its output into a constant-power-type source, which is beneficial for the inverter [11]. Therefore, two-stage conversion scheme is used in this thesis by implementing the DC-DC converter with MPPT as a part of whole control scheme.

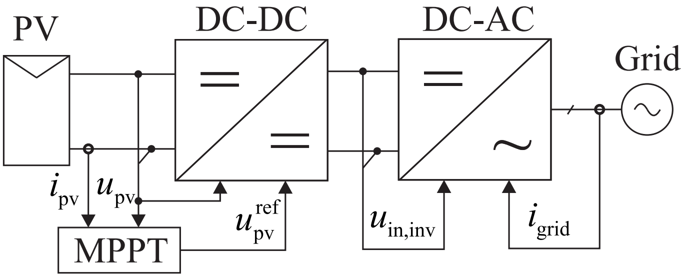

Figure 3.2: Two-stage PV conversion scheme. [11]

The input-voltage control in DC-DC converter is usually preferred over a current control. The problem with current control is the fact that a sudden change in the output current of the PVG due to irradiance change can saturate the controller. That causes the operating point to deviate away from MPP, toward the short-circuit operating point i_{sc}. In contrast, MPP voltage variance in changing irradiance is not as aggressive as current variation. Moreover, the voltage of PV generator is mainly affected by ambient temperature as discussed earlier. Since rapid temperature changes do not exist very often, voltage control is mainly used in PV applications. [12]

To optimize the operation of MPPT algorithms, the dynamical behavior of DC-DC converter need to be known. A switched-mode DC-DC converter is inherently nonlinear system due to different sub-circuits introduced by the switching actions. The number of these sub-circuits determines the operation mode of the converter. Therefore, the non-linearity of the semi-conductive components is typically taking into account by replacing the components with linear circuit elements at specific operating point. [13]

In order to analyze the operation of switched-mode converter, a linear model for the converter is required. The usual way is to use state-space averaging approach, which produce a linear small-signal model describing behavior between defined inputs and outputs in frequency domain around the specific operating point. Once the system behavior in frequency domain is known, the circuit response can be predicted related to changes in operation conditions. In this way, stable and controlled operation of a system can be guaranteed. [14] The following sections discuss the analysis of boost-power-stage converter by using state-space modeling technique.

3.1 Basic operation

The main idea of the boost converter is to increase the magnitude of input DC voltage in respect to the output voltage, which is performed by storing energy to the inductor. The converter is designed to operate in continuous conduction mode (CCM), where inductor current is either increasing or decreasing but never reaches zero. The main circuit diagram of the boost converter with additional input capacitor and parasitic elements can be seen in Fig. 3.3.

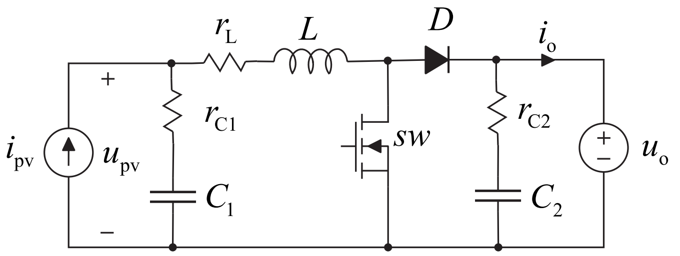

Figure 3.3: Power stage of a current-fed DC-DC boost converter with an added input-capacitor

The state-space averaging process starts with defining the different sub-circuits introduced by the switching action and calculating the average model of each sub-circuits. Due to the fact that the converter operates in CCM, the switching period T_s is divided into on-time and off-time sub-circuits defined by duty ratio d, which are represented in Fig. 3.4. When the switch is conducting in Fig. 3.4a, the input-voltage appears across the inductor and flowing current increases the energy stored in the magnetic field of the inductor. In contrast, when the switch is not conducting in Fig. 3.4b, the sum of the stored energy in the inductor and the energy from input source is fed to the output via a diode resulting in decreasing inductor current.

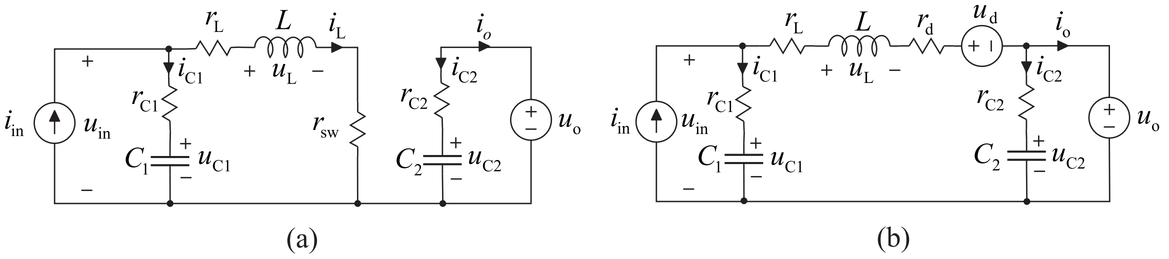

Figure 3.4: On-time (a) and off-time (b) subcircuits of the converter.

As can be concluded from Fig. 3.3, the input current and output voltage of the converter are determined externally, which means that they are the input variables of the system. In contrast, input voltage and output current of the converter are the outputs and can be affected by controlling the duty ratio. Therefore, they need to be solved as a function of other quantities. After applying Kirchoff's voltage and current laws to the circuit in Fig. 3.4, the averaged state-space representation in (3.1) can be obtained by multiplying the on-time equations with d and off-time equations with complement of duty ratio d' and summing them together.

$$
\begin{aligned}
\frac{d\left\langle i_{\mathrm{L}}\right\rangle}{dt} &= -\frac{r_{\mathrm{C1}}+r_{\mathrm{L}}+dr_{\mathrm{sw}}+d'r_{\mathrm{d}}}{L}\left\langle i_{L}\right\rangle+\frac{\left\langle u_{\mathrm{C1}}\right\rangle}{L}+\frac{r_{\mathrm{C1}}}{L}\left\langle i_{\mathrm{in}}\right\rangle-\frac{d'\left\langle u_{\mathrm{o}}\right\rangle-d'U_{\mathrm{d}}}{L}\\
\frac{d\left\langle u_{\mathrm{C1}}\right\rangle}{dt} &= \frac{\left\langle i_{\mathrm{in}}\right\rangle-\left\langle i_{\mathrm{L}}\right\rangle}{C_1}\\
\frac{d\left\langle u_{\mathrm{C2}}\right\rangle}{dt} &= \frac{\left\langle u_{\mathrm{o}}\right\rangle-\left\langle u_{\mathrm{C2}}\right\rangle}{C_2 r_{\mathrm{C2}}}\\
\left\langle u_{\mathrm{in}}\right\rangle &= r_{\mathrm{C2}}\left\langle i_{\mathrm{in}}\right\rangle-r_{\mathrm{C2}}\left\langle i_{\mathrm{L}}\right\rangle+r_{\mathrm{C2}}\left\langle u_{\mathrm{C1}}\right\rangle\\
\left\langle i_{\mathrm{o}}\right\rangle &= d'\left\langle i_{\mathrm{L}}\right\rangle+\frac{\left\langle u_{\mathrm{C2}}\right\rangle-\left\langle u_{\mathrm{o}}\right\rangle}{r_{\mathrm{C2}}}
\end{aligned}
\tag{3.1}
$$

Finally, the steady-state operation point can be solved by setting the derivative terms in (3.1) equal to zero and by substituting each variable with their upper-case steady-state values yielding

$$
\begin{aligned}
U_{\mathrm{in}} &= D'U_{\mathrm{o}}+(r_{\mathrm{L}}+Dr_{\mathrm{sw}}+D'r_{\mathrm{d}})I_{\mathrm{in}}+D'U_{\mathrm{d}}\\
D' &= \frac{U_{\mathrm{in}}-(r_{\mathrm{L}}+r_{\mathrm{sw}})I_{\mathrm{in}}}{U_{\mathrm{o}}+U_{\mathrm{d}}+(r_{\mathrm{L}}+r_{\mathrm{sw}})I_{\mathrm{in}}}\\
I_{\mathrm{L}} &= I_{\mathrm{in}}\\
U_{\mathrm{o}} &= U_{\mathrm{C2}}\\
U_{\mathrm{in}} &= U_{\mathrm{C1}}\\
I_{\mathrm{o}} &= D'I_{\mathrm{L}}.
\end{aligned}
\tag{3.2}
$$

3.2 Dynamic Modeling

In order to use mathematical tools, such as Laplace transformation, the averaged nonlinear model needs to be linearized. This is done by denoting the average values by a constant DC value summed with a small AC-perturbation. Mathematically, it is performed by using following formula

$$
\left.\frac{\partial f\left(x_1, x_2=X_2, ..., x_{\mathrm{n}}=X_{\mathrm{n}}\right)}{\partial x_1}\right|_{x_1=X_1}\cdot\hat{x}_1,
\tag{3.3}
$$

where each variable x_1 is first differentiated with itself and then the other variables are replaced with their corresponding steady-state values. Finally, variables of x_1 are replaced with steady-state values and the whole equation is multiplied with small signal variable $\hat{x}_1$. By using (3.1), (3.2) and (3.3), linearized state-space representation can be obtained as shown in (3.4).

$$
\begin{aligned}
\frac{\mathrm{d}\hat{\imath}_{\mathrm{L}}}{\mathrm{d}t} &= -\frac{R_{\mathrm{eq}}}{L}\hat{\imath}_{\mathrm{L}} + \frac{1}{L}\hat{u}_{\mathrm{C1}} + \frac{r_{\mathrm{C1}}}{L}\hat{\imath}_{\mathrm{in}} - \frac{D'}{L}\hat{u}_{\mathrm{o}} + \frac{U_{\mathrm{eq}}}{L}\hat{d} \\
\frac{\mathrm{d}\hat{u}_{\mathrm{C1}}}{\mathrm{d}t} &= -\frac{1}{C_1}\hat{\imath}_{\mathrm{L}} + \frac{1}{C_1}\hat{\imath}_{\mathrm{in}} \\
\frac{\mathrm{d}\hat{u}_{\mathrm{C2}}}{\mathrm{d}t} &= -\frac{1}{r_{\mathrm{C2}}C_2}\hat{u}_{\mathrm{C2}} + \frac{1}{r_{\mathrm{C2}}C_2}\hat{u}_{\mathrm{o}} \\
\hat{u}_{\mathrm{in}} &= -r_{\mathrm{C1}}\hat{\imath}_{\mathrm{L}} + \hat{u}_{\mathrm{C1}} + r_{\mathrm{C1}}\hat{\imath}_{\mathrm{in}} \\
\hat{\imath}_{\mathrm{o}} &= D'\hat{\imath}_{\mathrm{L}} + \frac{1}{r_{\mathrm{C2}}}\hat{u}_{\mathrm{C2}} - \frac{1}{r_{\mathrm{C2}}}\hat{u}_{\mathrm{o}} - I_{\mathrm{in}}\hat{d},
\end{aligned}
\tag{3.4}
$$

where the merged resistance R_{eq} and voltage U_{eq} are defined as

$$
\begin{aligned}
R_{\mathrm{eq}} &= r_{\mathrm{C1}} + r_{\mathrm{L}} + Dr_{\mathrm{sw}} + D'r_{\mathrm{d}} \\
U_{\mathrm{eq}} &= \left[r_{\mathrm{D}} - r_{\mathrm{sw}}\right] I_{\mathrm{in}} + U_{\mathrm{o}} + U_{\mathrm{d}},
\end{aligned}
\tag{3.5}
$$

The linearized state-space model in (3.4) can be presented in the standard state-space form as in (3.6) and (3.7).

$$
\begin{bmatrix} \frac{\hat{\imath}_{\mathrm{L}}}{dt} \\ \frac{\hat{u}_{\mathrm{C1}}}{dt} \\ \frac{\hat{u}_{\mathrm{C2}}}{dt} \end{bmatrix}
=
\begin{bmatrix} -\frac{R_{\mathrm{eq}}}{L} & \frac{1}{L} & 0 \\ -\frac{1}{C_1} & 0 & 0 \\ 0 & 0 & -\frac{1}{r_{\mathrm{C2}}C_2} \end{bmatrix}
\begin{bmatrix} \hat{\imath}_{\mathrm{L}} \\ \hat{u}_{\mathrm{C1}} \\ \hat{u}_{\mathrm{C2}} \end{bmatrix}
+
\begin{bmatrix} \frac{r_{\mathrm{C1}}}{L} & -\frac{D'}{L} & \frac{U_{\mathrm{eq}}}{L} \\ \frac{1}{C_1} & 0 & 0 \\ 0 & \frac{1}{r_{\mathrm{C2}}C_2} & 0 \end{bmatrix}
\begin{bmatrix} \hat{\imath}_{\mathrm{in}} \\ \hat{u}_{\mathrm{o}} \\ \hat{d} \end{bmatrix}
\tag{3.6}
$$

$$
\begin{bmatrix} \hat{u}_{\mathrm{in}} \\ \hat{\imath}_{\mathrm{o}} \end{bmatrix}
=
\begin{bmatrix} -r_{\mathrm{C1}} & 1 & 0 \\ D' & 0 & \frac{1}{r_{\mathrm{C2}}} \end{bmatrix}
\begin{bmatrix} \hat{\imath}_{\mathrm{L}} \\ \hat{u}_{\mathrm{C1}} \\ \hat{u}_{\mathrm{C2}} \end{bmatrix}
+
\begin{bmatrix} r_{\mathrm{C1}} & 0 & 0 \\ 0 & -\frac{1}{r_{\mathrm{C2}}} & -I_{\mathrm{in}} \end{bmatrix}
\begin{bmatrix} \hat{\imath}_{\mathrm{in}} \\ \hat{u}_{\mathrm{o}} \\ \hat{d} \end{bmatrix}
\tag{3.7}
$$

Now the linearized state-space in (3.6) and (3.7) is in the standard state-space form as given in (3.8). Inductor current and capacitor voltages are the state variables, input current, duty ratio and output voltage are the input variables as well as input voltage and output current are the output variables, respectively. The time-domain state space in (3.8) can be solved in frequency domain by applying Laplace transform with zero initial conditions, which yields (3.9).

$$
\begin{aligned}
\frac{\mathrm{d}\hat{\boldsymbol{u}}(t)}{\mathrm{d}t} &= \mathbf{A}\hat{\boldsymbol{x}}(t) + \mathbf{B}\hat{\boldsymbol{u}}(t) \\
\hat{\boldsymbol{y}}(t) &= \mathbf{C}\hat{\boldsymbol{x}}(t) + \mathbf{D}\hat{\boldsymbol{u}}(t)
\end{aligned}
\tag{3.8}
$$

$$\begin{aligned} s\boldsymbol{X}(s) &= \mathbf{A}\boldsymbol{X}(s) + \mathbf{B}\boldsymbol{U}(s) \\ \boldsymbol{Y}(s) &= \mathbf{C}\boldsymbol{X}(s) + \mathbf{D}\boldsymbol{U}(s) \end{aligned} \tag{3.9}$$

Solving the relation between input and output variables from (3.9) yields

$$\boldsymbol{Y}(s) = (\mathbf{C}(s\mathbf{I} - \mathbf{A})^{-1}\mathbf{B} + \mathbf{D})\boldsymbol{U}(s) = \mathbf{G}\boldsymbol{U}(s), \tag{3.10}$$

Matrix **G** in (3.10) contains six transfer functions, describing the mapping between input variables ($\boldsymbol{U} = [\hat{i}_{\text{in}}\ \hat{u}_{\text{o}}\ \hat{d}]^{\text{T}}$) and output variables ($\boldsymbol{Y} = [\hat{u}_{\text{in}}\ \hat{i}_{\text{o}}]^{\text{T}}$) Furthermore, (3.10) describes how to calculate the transfer functions when linearized state-space matrices are solved. Using matrix notation, the mapping can be expressed as follows

$$\begin{bmatrix} \hat{u}_{\text{in}} \\ \hat{i}_{\text{o}} \end{bmatrix} = \begin{bmatrix} Z_{\text{in-o}} & T_{\text{oi-o}} & G_{\text{ci-o}} \\ G_{\text{io-o}} & -Y_{\text{o-o}} & G_{\text{co-o}} \end{bmatrix} \begin{bmatrix} \hat{i}_{\text{in}} \\ \hat{u}_{\text{o}} \\ \hat{d} \end{bmatrix}. \tag{3.11}$$

The transfer functions Z_{in} and Y_{o} in (3.11) describe the ohmic characteristics of input and output terminals, respectively. The minus sign in the transfer function $Y_{\text{o-o}}$ is required since the current flowing out of the converter is defined positive. Without the correction, the transfer functions yield wrong results. The reverse-voltage transfer function T_{oi} describes the effect caused by the output voltage on the input voltage. Respectively, the control-to-input transfer function G_{ci} determines the interaction between control variable and input voltage, whereas G_{co} is interaction of control variable to the output current. Finally, the forward transfer-function G_{io} describes the effect caused by the input current to the output current. The subscript extension '-o' in each transfer function denote open-loop transfer functions.

As a graphical representation, the transfer function set (3.11) can be equally represented by linear two-port model as shown inside the dotted line in Fig. 3.5. The input port is modeled as a series connection of two dependent voltage sources and an input impedance, whereas the output port is modeled as a parallel connection of two dependent current sources and an output admittance.

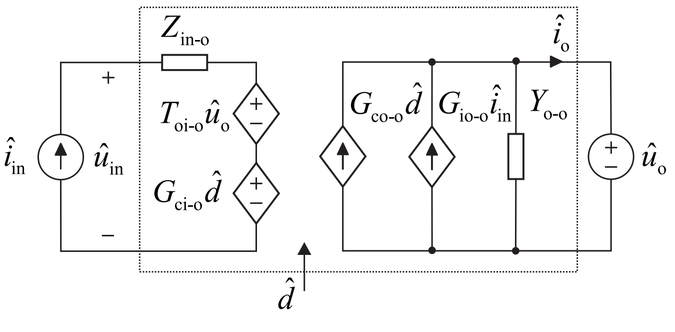

Figure 3.5: Linear two-port model of CF-CO converter with ideal source.

The symbolically expressed open-loop transfer functions of the converter are as follows:

$$
\begin{aligned}
Z_{\text{in-o}} &= \frac{1}{LC_1}\left(R_{\text{eq}} - r_{\text{C1}} + sL\right)\left(1 + sr_{\text{C1}}C_1\right)\frac{1}{\Delta} \\
T_{\text{oi-o}} &= \frac{D'}{LC_1}\left(1 + sr_{\text{C1}}C_1\right)\frac{1}{\Delta} \\
G_{\text{ci-o}} &= -\frac{U_{\text{eq}}}{LC_1}\left(1 + sr_{\text{C1}}C_1\right)\frac{1}{\Delta} \\
G_{\text{io-o}} &= -\frac{D'}{LC_1}\left(1 + sr_{\text{C1}}C_1\right)\frac{1}{\Delta} \\
G_{\text{co-o}} &= -I_{\text{in}}\left(s^2 - s\left(\frac{D'U_{\text{eq}}}{LI_{\text{in}}} - \frac{R_{\text{eq}}}{L}\right) + \frac{1}{LC_1}\right)\frac{1}{\Delta} \\
Y_{\text{o-o}} &= \frac{D^{'2}}{L}\frac{s}{s^2 + s\frac{R_{\text{eq}}}{L} + \frac{1}{LC_1}} + \frac{sC_2}{1 + sr_{\text{C2}}C_2},
\end{aligned}
\tag{3.12}
$$

where the determinant of the transfer functions, denoted by Δ, is

$$
\Delta = s^2 + s\frac{R_{\text{eq}}}{L} + \frac{1}{LC_1}. \tag{3.13}
$$

According to (3.12) and (3.13), the concerned converter has second order dynamic with resonance frequency appearing at an angular frequency of $1/\sqrt{LC_1}$.

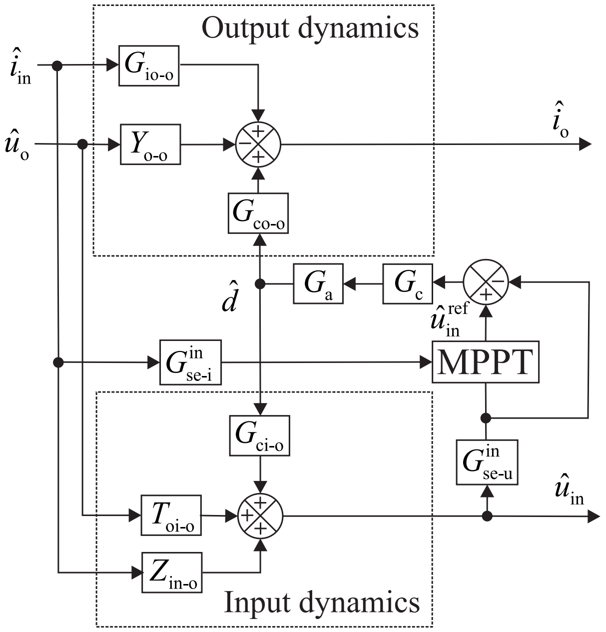

Figure 3.6: Control-block diagram of the input-voltage-controlled converter.

Another useful representation, in addition to the two-port model, is the control block diagram in Fig. 3.6, which can be derived from (3.11). To analyze operation of feedback-controlled converter, the closed-loop transfer functions can be solved from the open-loop control block diagram, and are given in matrix form in (3.14).

$$\begin{aligned}\begin{bmatrix}\hat{u}_{\mathrm{in}}\\ \hat{i}_{\mathrm{o}}\end{bmatrix} &= \begin{bmatrix}Z_{\mathrm{in-c}} & T_{\mathrm{oi-c}} & G_{\mathrm{ri}}\\ G_{\mathrm{io-c}} & -Y_{\mathrm{o-c}} & G_{\mathrm{ro}}\end{bmatrix}\begin{bmatrix}\hat{i}_{\mathrm{in}}\\ \hat{u}_{\mathrm{o}}\\ \hat{u}_{\mathrm{in}}^{\mathrm{ref}}\end{bmatrix}\\ &= \begin{bmatrix}\dfrac{Z_{\mathrm{in-o}}}{1-L_{\mathrm{in}}} & \dfrac{T_{\mathrm{oi-o}}}{1-L_{\mathrm{in}}} & -\dfrac{1}{G_{\mathrm{se-u}}^{\mathrm{in}}}\dfrac{L_{\mathrm{in}}}{1-L_{\mathrm{in}}}\\ \dfrac{G_{\mathrm{io-o}}+G_{\mathrm{io-\infty}}L_{\mathrm{in}}}{1-L_{\mathrm{in}}} & -\dfrac{Y_{\mathrm{o-o}}+L_{\mathrm{in}}Y_{\mathrm{o-\infty}}}{1-L_{\mathrm{in}}} & \dfrac{1}{G_{\mathrm{se-u}}^{\mathrm{in}}}\dfrac{G_{\mathrm{co-o}}}{G_{\mathrm{ci-o}}}\dfrac{L_{\mathrm{in}}}{1-L_{\mathrm{in}}}\end{bmatrix}\begin{bmatrix}\hat{i}_{\mathrm{in}}\\ \hat{u}_{\mathrm{o}}\\ \hat{u}_{\mathrm{in}}^{\mathrm{ref}}\end{bmatrix},\end{aligned} \tag{3.14}$$

where

$$\begin{aligned}&\mathrm{L}_{\mathrm{in}} = G_{\mathrm{se-u}}^{\mathrm{in}}G_{\mathrm{c}}G_{\mathrm{a}}G_{\mathrm{ci-o}},\\ &G_{\text{io-}\infty} = G_{\text{io-o}} - \frac{Z_{\text{in-o}}G_{\text{co-o}}}{G_{\text{ci-o}}}, \quad Y_{\text{o-}\infty} = Y_{\text{o-o}} + \frac{T_{\text{oi-o}}G_{\text{co-o}}}{G_{\text{ci-o}}}.\end{aligned} \tag{3.15}$$

In (3.15), L_{in} is called input-voltage loop gain, $G_{\mathrm{se-u}}^{\mathrm{in}}$ is the input-voltage sensing gain, G_{c} is the input-voltage controller transfer function, G_{a} is the modulator gain, $G_{\text{io-}\infty}$ is ideal forward current gain and $Y_{\text{o-}\infty}$ is the ideal output admittance, respectively. The meaning of special transfer functions $G_{\text{io-}\infty}$ and $Y_{\text{o-}\infty}$ can be seen from $\mathrm{G}_{\mathrm{io-c}}$ and $Y_{\mathrm{o-c}}$ in (3.14) by examining the magnitude of the loop gain L_{in}. Typically, the control loop is designed to have a high gain at low frequencies to eliminate the steady-state error. This can be achieved by using a controller with integrator resulting theoretically infinite gain at low frequencies. The high loop gain at low frequencies yields that closed-loop transfer functions $\mathrm{G}_{\mathrm{io-c}}$ and $Y_{\mathrm{o-c}}$ equals ideal transfer functions $G_{\mathrm{io-\infty}}$ and $Y_{\mathrm{o-\infty}}$. In contrast, at high frequencies the loop gain is low and therefore, closed-loop transfer functions $Z_{\mathrm{in-c}}, T_{\mathrm{oi-c}}, G_{\mathrm{io-c}}$ and $Y_{\mathrm{o-c}}$ approach their corresponding open-loop transfer functions.

3.3 Effect of Nonideal Source

The non-idealities of source and load play a significant role in the behavior of a switched-mode converter. Therefore, in order to correctly model and predict the system operation, these effects have to be taken into account in the modeling. The transfer functions calculated in the previous section describe only the converter internal dynamics by assuming that the source and load are ideal. However, PVG is not ideal and thus its effect on the converter dynamics shall be taken into account. The operating-point-dependent dynamic effect of a PVG can be taken into account by considering the admittance Y_{S} parallel to the input current source as shown in Fig. 3.7.

To approximate the value for source admittance, the low-frequency value of source

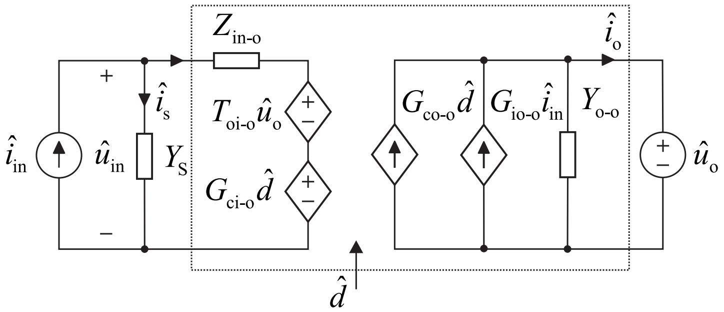

Figure 3.7: Linear two-port model of CF-CO converter with nonideal source.

impedance can be achieved by as follows

$$Z_S \approx r_s + r_d || r_{sh} = r_{pv}. \tag{3.16}$$

Now, the input current of the converter is the input current i_{inS} subtracted by the current through the admittance Y_S. When this new input current is substituted to (3.11), the source-affected transfer functions of the converter (3.17) can be solved as instructed in [15].

$$\begin{aligned}\begin{bmatrix} \hat{u}_{\text{in}} \\ \hat{i}_o \end{bmatrix} &= \begin{bmatrix} Z^S_{\text{in-o}} & T^S_{\text{oi-o}} & G^S_{\text{ci-o}} \\ G^S_{\text{io-o}} & -Y^S_{\text{o-o}} & G^S_{\text{co-o}} \end{bmatrix} \begin{bmatrix} \hat{i}_{\text{inS}} \\ \hat{u}_o \\ \hat{d} \end{bmatrix} \\ &= \begin{bmatrix} \dfrac{Z_{\text{in-o}}}{1+Y_S Z_{\text{in-o}}} & \dfrac{T_{\text{oi-o}}}{1+Y_S Z_{\text{in-o}}} & \dfrac{G_{\text{ci-o}}}{1+Y_S Z_{\text{in-o}}} \\ \dfrac{G_{\text{io-o}}}{1+Y_S Z_{\text{in-o}}} & -\dfrac{1+Y_S Z_{\text{in-oco}}}{1+Y_S Z_{\text{in-o}}} & \dfrac{1+Y_S Z_{\text{in-}\infty}}{1+Y_S Z_{\text{in-o}}} G_{\text{co-o}} \end{bmatrix} \begin{bmatrix} \hat{i}_{\text{inS}} \\ \hat{u}_o \\ \hat{d} \end{bmatrix},\end{aligned} \tag{3.17}$$

where $Z_{\text{in-oco}}$ denotes the impedance characteristics of the converter input when the output of the converter is open-circuited and $Z_{\text{in-}\infty}$ denotes certain ideal input impedance given in (3.18) and (3.19), respectively.

$$Z_{\text{in-oco}} = Z_{\text{in}} + \frac{G_{\text{io}} T_{\text{oi}}}{Y_o}, \tag{3.18}$$

$$Z_{\text{in-}\infty} = Z_{\text{in}} - \frac{G_{\text{io}} G_{\text{ci}}}{G_{\text{co}}} \tag{3.19}$$

3.4 The Converter Specification

The converter used in thesis is based on the converter design done in [16] with conventional design method. In such a method, the nominal power of the converter is selected by multiplying the nominal power $P_{\mathrm{pv,stc}}$ of the PVG by sizing factor SF, which is the ratio of solar inverter nominal power to the DC power $P_{\mathrm{pv,stc}}$ of a PVG in STC. The maximum input current $I_{\mathrm{pv,max}}$ was calculated by dividing the nominal power of the converter of the converter by the minimum input voltage $U_{\mathrm{mpp,min}}$ as following

$$I_{\mathrm{pv,max}} = \frac{P_{\mathrm{pv,stc}}SF}{U_{\mathrm{mpp,min}}}. \tag{3.20}$$

By using (3.20), the maximum input current used in the design was 22.9 A. In contrast, the maximum inductor current ripple was set to be 10 % of the maximum input current and the switching frequency was selected to be 100 kHz. Correspondingly, input capacitor was selected so that converter have at least 15 dB attenuation from the output voltage to the input voltage at the frequency of 100 Hz, input voltage ripple is low and the converter is stable with sufficient margins. The parameters of the converter are collected to the table in Appendix A (Tab. A.1). These values were also used in MPPT simulations.

Due to the fact that there is high peaking at resonant frequency in CC region, the additional damping circuit was added in parallel with the input capacitor. The reason for the high peaking is the high output impedance of the PV module in the CC region, low ESR value of the input capacitor and low DC resistance value of the inductor. The designed damping circuit consist of series connected resistor and capacitor and the values were selected to equal the characteristic impedance $Z_{\mathrm{o}} = \sqrt{L/C_1}$ of the converter resonant circuit. The damping circuit can be taken into account in model by adding damping network admittance to the source admittance. The final closed-loop transfer functions can be calculated based on the source-affected open-loop transfer functions similarly as done with ideal source. Including the effect of damping circuit, the Matlab$^{\mathrm{TM}}$ Simulink model of the boost converter was constructed based on the on-time and off-time equations.

4. MAXIMUM POWER POINT TRACKING

The performance of MPPT is one of the most important concerns in any PV system and it has been observed to have significant contribution to the reliability problems in photovoltaic energy systems [17]. In order to obtain maximum amount of energy from PVG, the operation point need to be forced to be at the MPP. This can be done by implementing a MPPT to PV system, which ensures that the operation point is kept at maximum power point in all environmental conditions utilizing all the extracted power from PVG.

Over the past decades, many MPPT techniques have been published and they vary in complexity, sensors required, convergence speed, cost, range of effectiveness and implementation hardware [2, 18]. The most of the developed MPPT techniques usually measure both voltage and current values. Temperature and irradiance sensors are usually avoided due to their high costs, especially in large PV plants where each panel requires own sensor. These techniques, on the other hand, can usually only track the local maximum power point. Moreover, the appearance of multiple MPPs on PVG characteristics have created a requirement to develop MPPT algorithms that can separate real, global maximum power point from the multiple local maximum power points.

MPPT can be implemented either by using analog or digital circuitry. Although, some analog implementations are still developed [19], they are not widely utilized in PV applications due to the fact that it is difficult to take into account the tolerances and parametric drifts [20, p. 40]. Moreover, the control system of modern converter is usually implemented digitally, thus, as the simplest MPPT can be implemented with a few lines of code only. The simplest algorithms can be designed with microcontrollers, whereas the more advanced techniques require digital signal processors (DSP) or field-programmable gate array (FPGA) systems due to their high computational burden. Typically, those systems are based on soft computing such as neural network or fuzzy logic.

This chapter is organized as follows: First a brief overview of most widely used MPPT algorithms is given. Then perturbative algorithms are discussed in more detail in respect to system configuration under different atmospheric conditions. At the end of the chapter, some improvements for the traditional perturbative algorithm are presented.

4.1 Overview of Most Popular Methods

4.1.1 Indirect Techniques

The developed MPPT techniques can be divided into indirect and direct technique referring to the method, how MPP is evaluated. The indirect methods are based on the prior knowledge of the PV generator and they do not usually measure the extracted power directly from PVG. In contrast, they estimate the MPP based on a single measurement of voltage or current with predefined data from PVG. Due to the fact that the MPP is determined by predefined mathematical models, MPP can be only approximately tracked. Therefore, significant errors can occur in MPPT if atmospheric conditions deviate too much from those predicted in models reducing the extracted energy yield from PVG. However, most of the indirect MPPT techniques are suitable for low-cost applications, since complex hardware is not required.

The constant voltage method, known as fractional open-circuit method, is one of the simplest MPPT methods. It is based on the observation that the MPP voltage is relatively close to a fixed percentage of the OC voltage. OC voltage can be then measured in certain time intervals and the operation point can adjusted based on the measurement. [21] The problem is to find a proper coefficient to describe the relation between MPP and OC voltage, since the same coefficient does not hold for all operational conditions and PV panels. It has been shown that such coefficient varies between 0.78 and 0.92 depending on the characteristics of the PVG [18]. Although the proper coefficient is found, it cannot be guaranteed that the system is working at MPP, since the fixed percentage of the OC voltage is only approximation of real MPP voltage. Moreover, a small amount of energy is lost, when system is open-circuited and the new MPP voltage value is calculated decreasing the overall efficiency of the system. However, the technique is suitable for small PV generators, where it is easy to implement and cost-effective.

The more intelligent indirect MPPT techniques are based on more detailed data from the PV panel such as look-up table and curve-fitting techniques. In look-up table technique, the measured voltage and current values of the PVG are compared with those stored in the control system. Based on the saved data, the operation point is forced to the predetermined MPP. The look-up table is rather simple MPPT technique and it is able to perform fast tracking, since a new MPP is instantly known as an optimum case. As a disadvantage of this technique, large capacity of memory is required for storing data, especially, in cases where good accuracy is important. However, it is not possible to record and store the data from all the atmospheric conditions. [22]

The curve-fitting requires more computational burden rather than large memory capacity. On this method, the nonlinear behavior of PV cell is calculated by using mathematical models. For example, following third-order polynomial is used in curve-fitting technique to characterize the P-U curve [18]

$$p_{\mathrm{pv}} = Au_{\mathrm{pv}}^3 + Bu_{\mathrm{pv}}^2 + Cu_{\mathrm{pv}} + D, \tag{4.1}$$

where the coefficients A, B, C and D are determined by sampling of PV voltage u_{pv} and power p_{pv} in intervals. Since the power voltage derivative is zero at the MPP, (4.1) shrinks to a second-order derivative and MPP voltage can be calculated by using a quadratic formula. For accurate MPP tracking, this procedure should be repeated in certain time intervals. However, the disadvantage of this method is that it requires accurate knowledge of the physical parameters related to the cell material and manufacturing specifications are not valid for all atmospheric conditions. [23]

4.1.2 Direct Techniques

In PV system, where high MPPT efficiency is important in all environmental conditions, direct MPPT methods are more preferred over the indirect methods. Such methods, also known as true seeking methods, include techniques that use voltage and current measurements of PVG for tracking the MPP. These techniques have an advantage of being independent from the prior knowledge of the PVG characteristics. Due to independent operation, direct methods usually achieve better performance compared to indirect methods in varying atmospheric conditions.

Perturb-based MPPT techniques are most widely utilized in PV applications. The basic form of perturbative algorithm is perturb and observe (P&O) and incremental conductance techniques (IC), which are based on the injection of small perturbation into the system and observing the effect to locate the MPP. After the MPP is reached, the operation point is oscillating around the MPP causing mismatch losses by natural behavior of the algorithm. Moreover, it have been discovered that the conventional P&O algorithm can be confused during the rapidly changing irradiance conditions [24]. To overcome such drawbacks, some improvements to the conventional technique have been developed. Furthermore, more intelligent perturb-based algorithms have been introduced such as particle swarm optimization, extrenum seeking and the self-oscillation method. Basically, these methods differ from the basic P&O approach either for the variable observed or for the type of perturbation.

Particle swarm optimization (PSO) is a population-based stochastic optimization technique. Since the PSO method uses search optimizion for nonlinear functions, theoretically, it should be able to locate the MPP for any type of P-U curve regardless the environmental conditions. The main idea over the traditional P&O is to reduce the steady-state oscillation around the MPP. This is done by designing the particle velocity so that its value is close to zero when the system operation approaches the MPP, whereas control of a DC-DC converter approaches its constant value. However, the tuning of the design parameters has a huge effect on performance of the technique. Once the parameters are properly chosen for a specific system, it has been shown that

PSO is effective even partial shading conditions with multiple MPPs. [25]

Extremum seeking (ES) and the ripple correlation control (RCC) techniques are based on the detection of low and high-frequency oscillating components of a converter, respectively. In grid-connected PV applications, DC-link voltage fluctuation can end up to PVG terminals, where ES can use the 100 Hz voltage ripple component for tracking the MPP. Using the information that the amplitude of sinusoidal disturbance minimizes at MPP, the operation point can be forced to MPP by observing the amplitude of the ripple. [26] In contrast, RCC utilizes the high-frequency ripple generated by the switching action to perform MPPT. Since the time derivative of the power is related to the time derivative of the current or of the voltage, the power gradient is driven to zero indicating that the operation point matches the MPP. [27]

In addition to the perturbative algorithms, increasing computational performance have made the soft computing methods such as fuzzy logic and neural network popular for MPPT over the last decade in different PV applications [2, 18]. The advantage of such techniques is that they handle the nonlinearity well and therefore, they are very suitable for nonlinear power maximization task. Unfortunately, general rules how to select optimal values does not exist. In fuzzy logic controllers, the performance is highly depended on choosing the right error computation and rule base table. Therefore, a lot of knowledge is needed in choosing right parameters to ensure optimal operation. Moreover, the neural network strategies require specific training for each type of PVG since the input variables can be any of the PV cell parameters such as open-circuit voltage, short-circuit current or atmospheric data, for instance.

4.1.3 Global Maximum Power Point Tracking

Most of introduced MPPT techniques in previous sections are only able to track a local MPP, since they are designed to find the closest MPP in respect to a present operation point. However, in partial shading conditions multiple MPPs can occur on the electrical characteristics of the PV generator. Thus the local MPPT algorithms cannot distinguish the local MPP from the global one yielding reduced energy yield [28]. This is a problem especially in the cases, where the global MPP is at lower voltage yielding the higher voltage difference between the unshaded and partially shaded situation. Therefore, there has been a lot of research related to the development of global algorithms.

The global MPPT algorithms are typically based on scanning the whole P-U curve and then alternatively using a local MPPT algorithms such as perturbative algorithms for fine adjusting [29]. The scanning can be performed by using the current sweep method to sweep the operation point from open-circuit to short-circuit condition. The major disadvantage is that energy is lost every time the search is performed. The more intelligent approaches to perform P-U curve scanning can be done when utilizing the knowledge about the system and operation conditions. For example, the proposed method in [30] uses the information that the minimum distance between two local MPPs is the MPP voltage of the shaded series-connected PV cells connected in anti-parallel with a bypass diode.

4.2 Analysis of Perturbative Algorithms

Perturb and Observe (P&O) technique is the most popular MPPT algorithm. It is widely adopted due to its simplicity, ease of implementation and good performance [31]. Classification of two different P&O techniques can be seen in Fig. 4.1. In a traditional fixed-step P&O technique, the perturbed variable x is either duty ratio or voltage depending on the control scheme. The prior scheme, also called hill climbing method, controls a converter directly by the duty ratio generated by MPPT. In the latter scheme, MPPT produces the input voltage reference for the voltage controller, which generates the duty ratio value. The both control schemes are discussed in the following sections.

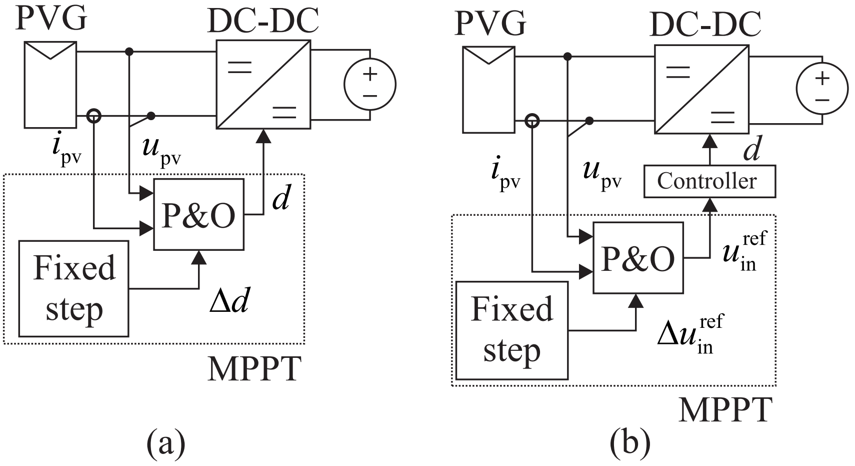

Figure 4.1: Open-loop (a) and closed-loop (b) perturb-based algorithm control scheme

The P&O operation principle is rather simple. As the name of the algorithm reveals, P&O technique is based on perturbing the PVG operating point periodically by changing the output voltage of the PV generator with perturbation step Δx and observing the effect in PVG output terminal. Before every perturbation, the power $P_{\text{pv}}(k)$ is measured at present time instant k by using voltage and current measurement. The calculated power is then compared to the power $P_{\text{pv}}(k-1)$ measured on the previous perturbation period. If the power change is positive, i.e. power is increasing, the sign of the next perturbation is kept the same. Otherwise, in case of decreased power, direction of the next perturbation step is reversed indicating the wrong direction. The algorithm is performed after every user-defined sampling period T_{p}. A flowchart of the algorithm is presented in Fig. 4.2.

A similiar technique is the incremental conductance (IC) method, which was first presented in [32]. As the traditional P&O technique, IC is also based on the direction of power. While the P&O algorithms uses two consecutive power measurements for power prediction, the IC method uses conductance and incremental conductance for power prediction. IC technique is based on the observation that at MPP the following

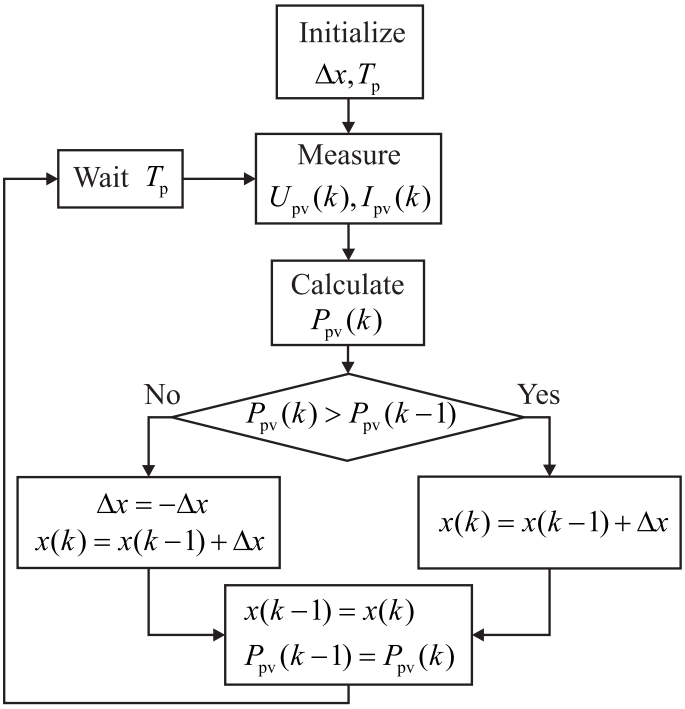

Figure 4.2: The flowchart of fixed-step P&O algorithm. The perturbed variable x is either duty ratio or voltage depending on implementation.

equation is valid

$$\frac{\Delta p_{\text{pv}}}{\Delta u_{\text{pv}}} = \frac{\Delta(u_{\text{pv}} i_{\text{pv}})}{\Delta u_{\text{pv}}} = I_{\text{pv}} + U_{\text{pv}} \frac{\Delta i_{\text{pv}}}{\Delta u_{\text{pv}}} = 0, \tag{4.2}$$

which can be represented as

$$\frac{I_{\text{pv}}}{U_{\text{pv}}} = -\frac{\Delta i_{\text{pv}}}{\Delta u_{\text{pv}}}. \tag{4.3}$$

Eq. (4.3) corresponds to the situation, where the absolute value of conductance equals to the absolute value of the incremental conductance. Comparing these two conductances, the sign of the next perturbation can be determined. If the operation point is at the left side of the P-U curve respect to the MPP, conductance value is higher than incremental conductance. Therefore, the voltage of the PVG must be increased to convergence to the MPP. Similarly, if the conductance is smaller than incremental conductance, the MPP is at lower voltage level i.e. the voltage of the PVG must be decreased. If the conductance equals the incremental conductance, the operation point locates at a MPP and perturbation on either direction is not required. The correlation of conductance and incremental conductance in different operation points is also represented in Fig. 4.3.

However, the condition in (4.3) only applies for ideal systems and there is no such a condition in practice due to noise and quantization effects in real implemented systems [33]. Therefore, a predetermined threshold should be used to detect when operation

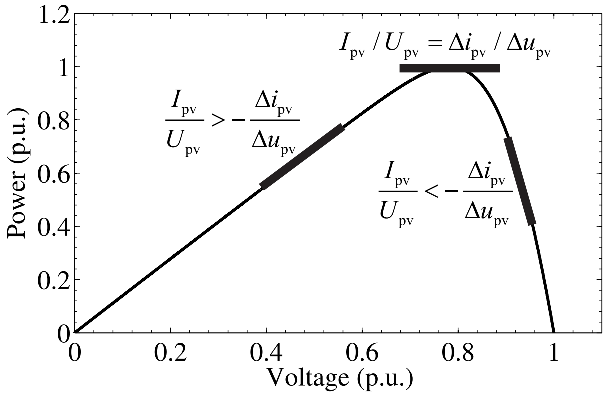

Figure 4.3: Correlation of conductance and incremental conductance in three different locations on P-U curve.

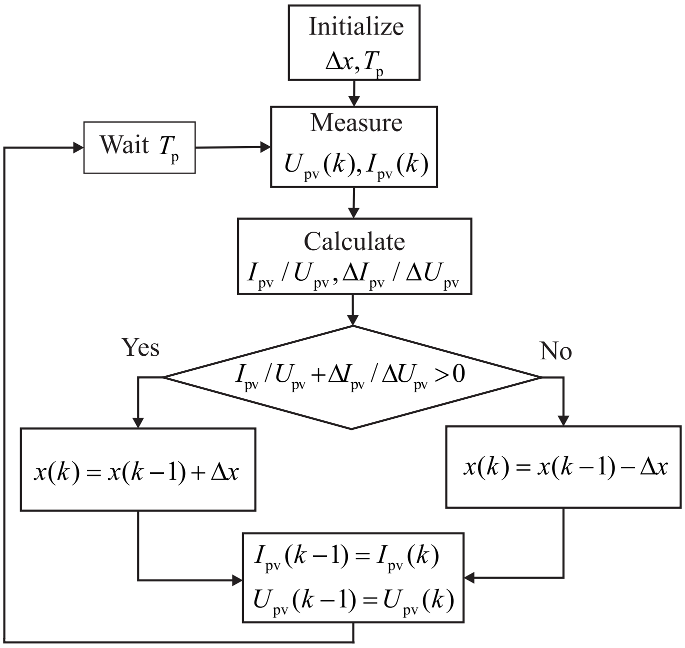

Figure 4.4: A flowchart of the incremental conductance technique.

point locates at MPP within predefined tolerance. However, the same kind of threshold can be designed for P&O algorithm as well, thus, the incremental conductance cannot be said to be more preferable compared to the P&O method.

Furthermore, the IC method is usually assumed to improve steady-state and dynamic performance of the P&O algorithm [23, 34, 35]. However, it has been shown that there is no practical difference in performance between these two methods when both algorithms are properly optimized [33, 36]. In fact, the only difference is numerical calculation of derivatives in IC method. Therefore, using incremental conductance method, the step size can be defined a little lower than in P&O method to achieve similar dynamic performance in rapid changing atmospheric conditions. Although, the incremental conductance method requires a little bit more computational burden compared to the P&O method due to derivative calculations, it is not an issue even for modern microcontrollers. However, analyzing the operation of P&O algorithm is more straightforward and therefore the following sections describe the optimization of

P&O algorithms, only. Nevertheless, the same optimization principles are valid for all perturbative algorithms as well.

4.2.1 Steady-State Operation

In stable steady-state operation, where atmospheric conditions remain constant, the P&O algorithm has three different operation points as shown in Fig. 4.5. In such ideal condition, the middle operation point is at MPP and the others are on both sides of the MPP as illustrated in Fig. 4.5a. Moreover, as can be seen in Fig. 4.5b, the period of P&O algorithm waveform is $4T_\mathrm{p}$ with peak-to-peak amplitude of $2\Delta U_\mathrm{pv}$. Such a stable operation can be ensured by selecting proper values of Δx and T_p yielding to the highest MPPT efficiency.

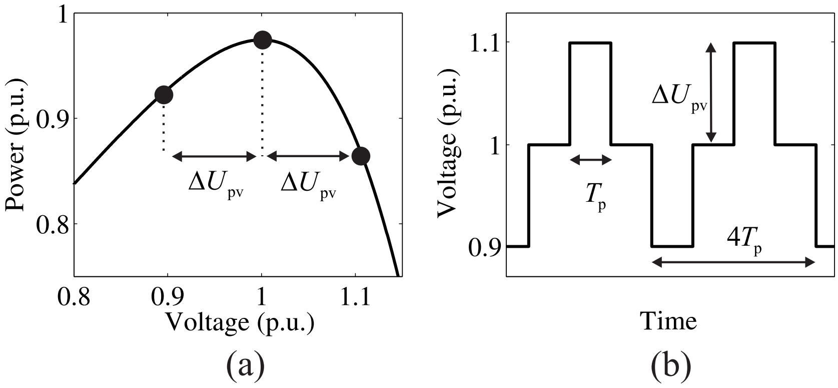

Figure 4.5: Operation of perturbative MPPT algorithm in constant atmospheric condition (a) with ideal voltage waveform (b).

Although the first use of P&O algorithm goes back to 1970s in space applications, any general guidelines how the sampling time and perturbation step size should be chosen for PV applications did not exit until in [24]. Before that, the tracking algorithms normally used in inverters have speeds ranging approximately between 0.1 % of U_mpp/s and 1.0 % of U_mpp/s [37]. However, such simplified design rules do not optimize the sampling time and perturbation step size in respect to implemented system. In contrast, [24] proposes design rules for choosing the fastest sampling and the minimum step size without compromising the proper operation of the system in steady-state and dynamic atmospheric conditions. The objective of the next two sections is to introduce and simulate those design rules in practice.

The sampling interval T_p is one of the two design parameters in fixed-step perturbative algorithms. Such techniques use typically fixed sampling period, which is defined before system startup. To achieve fast response in dynamic conditions, T_p must be set as short as possible without causing instability in MPPT operation. This instability can occur when the algorithm samples voltage and current too quickly yielding to incorrect measurements by the transient behavior of the whole system. Since, the power samples are not reliable, three point operation as represented in Fig. 4.5b cannot be guaranteed in every circumstances reducing the energy yield. [24]

In general, the sampling time must be selected higher than the system settling time to ensure stability. In addition, the optimization of P&O variables become easier when non-oscillating behavior is assumed at the moment of a new measurement. Since the perturbative algorithms are based on derivative of power, sampling time of the algorithms need to be selected based on transient behaviour of PVG power. This can be done by constituting small signal variation of power $\hat{p}_{\mathrm{pv}}$. If considering small voltage and current oscillations u_{pv}, i_{pv} compared to steady-state MPP values U_{mpp}, I_{mpp}, the relationship between u_{pv}, i_{pv}, G and T can be linearized by using (3.3):

$$\hat{i}_{\mathrm{pv}} = \left.\frac{\partial i_{\mathrm{pv}}}{\partial u_{\mathrm{pv}}}\right|_{\mathrm{MPP}} \hat{u}_{\mathrm{pv}} + \left.\frac{\partial i_{\mathrm{pv}}}{\partial G}\right|_{\mathrm{MPP}} \hat{G} + \left.\frac{\partial i_{\mathrm{pv}}}{\partial T}\right|_{\mathrm{MPP}} \hat{T}, \tag{4.4}$$

where symbols with hats represent the small-signal variations around the steady-state values of the corresponding quantities. In steady-state conditions, irradiance is constant and $\hat{G} = 0$. Furthermore, due to relatively high thermal inertia of a PVG, temperature of PVG can be assumed to be constant between perturbations i.e. $\hat{T} = 0$. The partial derivative $\partial i_{\mathrm{pv}}/\partial u_{\mathrm{pv}}$ represent the incremental or dynamic conductance corresponding inverse value of dynamic resistance. When operating near the MPP, dynamic resistance equals static MPP resistance. Thus the effect of partial derivate $\partial i_{\mathrm{pv}}/\partial u_{\mathrm{pv}}$ in (4.4) can be simplified as follows

$$\hat{i}_{\mathrm{pv}} \approx \frac{\hat{u}_{\mathrm{pv}}}{R_{\mathrm{mpp}}}. \tag{4.5}$$

For the operation point close to MPP, the voltage is $u_{\mathrm{pv}} = U_{\mathrm{mpp}} + \hat{u}_{\mathrm{pv}}$ and the current $i_{\mathrm{pv}} = I_{\mathrm{mpp}} + \hat{i}_{\mathrm{pv}}$ and therefore power can be represented as

$$p_{\mathrm{pv}} = P_{\mathrm{mpp}} + \hat{p}_{\mathrm{pv}} = U_{\mathrm{mpp}} I_{\mathrm{mpp}} + U_{\mathrm{mpp}} \hat{i}_{\mathrm{pv}} + I_{\mathrm{mpp}} \hat{u}_{\mathrm{pv}} + \hat{u}_{\mathrm{pv}} \hat{i}_{\mathrm{pv}}. \tag{4.6}$$

From (4.5), (4.6) and using $U_{\mathrm{mpp}} = R_{\mathrm{mpp}} I_{\mathrm{mpp}}$ and $P_{\mathrm{mpp}} = U_{\mathrm{mpp}} I_{\mathrm{mpp}}$, perturbed power $\hat{p}_{\mathrm{pv}}$ can be represented as a function of voltage $\hat{u}_{\mathrm{pv}}$ and R_{mpp} as follows

$$\begin{aligned} \hat{p}_{\mathrm{pv}} &= U_{\mathrm{mpp}} \hat{i}_{\mathrm{pv}} + \hat{u}_{\mathrm{pv}} I_{\mathrm{mpp}} + \hat{u}_{\mathrm{pv}} \hat{i}_{\mathrm{pv}} \\ &= \hat{u}_{\mathrm{pv}} \left(I_{\mathrm{mpp}} - \frac{U_{\mathrm{mpp}}}{R_{\mathrm{mpp}}} \right) + \hat{u}_{\mathrm{pv}} \hat{i}_{\mathrm{pv}} \approx -\frac{\hat{u}_{\mathrm{pv}}^2}{R_{\mathrm{mpp}}}. \end{aligned} \tag{4.7}$$

Eq. (4.7) reveals that the behavior of power variation $\hat{p}_{\mathrm{pv}}$ at the PVG output can be analyzed by observing small signal variation of PVG voltage $\hat{u}_{\mathrm{pv}}$. According to (4.7), the only difference between the power and voltage characteristics of PV generator is the DC gain $1/\mathrm{R}_{\mathrm{mpp}}$ yielding to the same dynamics for the $\hat{u}_{\mathrm{pv}}^2$ and $\hat{p}_{\mathrm{pv}}$. However, the effect of DC gain need to be taken into account when analyzing the settling time of the step response. When assuming stationary environmental conditions, PVG voltage transient can be represented by

$$\hat{u}_{\mathrm{pv}} = G^{\mathrm{S}}_{\mathrm{ci-o}}\hat{d} + T^{\mathrm{S}}_{\mathrm{oi-o}}\hat{u}_{\mathrm{o}}. \tag{4.8}$$

Moreover, if the output voltage is assumed constant (i.e. $\hat{u}_{\mathrm{o}} \approx 0$), the behavior of input voltage can be analyzed by observing only the control-to-input voltage transfer function. According to the basic control system theory, the second-order transfer function can be presented as

$$G_{\mathrm{ci-o}}(s) = \frac{\hat{u}_{\mathrm{pv}}}{\hat{d}} = \frac{K\omega_{\mathrm{n}}^2}{s^2 + 2\zeta\omega_{\mathrm{n}}^2 s + \omega_{\mathrm{n}}^2}, \tag{4.9}$$

where K is the DC gain, ω_{n} is natural angular frequency, and ζ is the damping factor. Damping factor ζ provides a mathematical means of expressing the level of damping in a system relative to critical damping and it can achieve values between zero to one. The higher the damping factor is the faster the decaying oscillatory behavior is attenuated. The damping factor $\zeta = 0$ corresponds to the sinusoidal oscillatory case without decay, whereas the condition $\zeta = 1$ refers the system which is critically damped.

Applying average state-space modeling technique to the boost converter with constant-voltage load and without parasitic elements, the following source-affected control-to-input transfer function can be obtained from (3.17)

$$G^{\mathrm{S}}_{\mathrm{ci-o}}(s) = \frac{\hat{u}_{\mathrm{pv}}}{\hat{d}} = \frac{U_{\mathrm{o}}}{LC_1\left(s^2 + \frac{1}{C_1 r_{\mathrm{pv}}}s + \frac{1}{LC_1}\right)}. \tag{4.10}$$

Now it can be seen that damping ratio is

$$\zeta = \frac{1}{2r_{\mathrm{pv}}}\sqrt{\frac{L}{C_1}}. \tag{4.11}$$

If the parasitic elements are taken into account, the high-frequency zero appears at angular frequency $\omega_{\mathrm{z}} = 1/r_{\mathrm{C1}}C_1$ in the control-to-input voltage transfer function. This increases the damping factor with additional term yielding the new formula for damping factor

$$\zeta = \frac{1}{2r_{\mathrm{pv}}}\sqrt{\frac{L}{C_1}} + \frac{r_{\mathrm{C1}} + r_{\mathrm{L}}}{2}\sqrt{\frac{C_1}{L}}. \tag{4.12}$$

The high-frequency zero decreases the settling due to the fact that oscillation in the transient response is more attenuated. However, the effect of high-frequency zero is usually low and therefore (4.11) gives a good approximation for damping factor. The undamped natural angular frequency of the converter can be presented as

$$\omega_\mathrm{n} = \frac{1}{\sqrt{LC_1}}. \tag{4.13}$$

Eq. 4.10 can be represented in time domain as voltage $\hat{u}_\mathrm{pv}(t)$ step response by performing the inverse Laplace transform.

$$\hat{u}_\mathrm{pv}(t) = U_\mathrm{o}\Delta d \left(1 - \frac{1}{\sqrt{1-\zeta^2}} \exp(-\zeta\omega_\mathrm{n}t) \sin\left(\omega_\mathrm{n}t\sqrt{1-\zeta^2} + \arccos\left(\zeta\right)\right)\right). \tag{4.14}$$

Since power $\hat{p}_\mathrm{pv}(t)$ at the MPP can be approximated with $\hat{u}_\mathrm{pv}(t)$ and R_mpp in (4.7), step response for power can be rewritten as

$$\begin{aligned} \hat{p}_\mathrm{pv}(t) &= -\frac{\hat{u}^2_\mathrm{pv}(t)}{R_\mathrm{mpp}} \\ &= -\frac{U_\mathrm{o}^2\Delta d^2}{R_\mathrm{mpp}} \left(1 - \frac{1}{\sqrt{1-\zeta^2}} \exp\left(-\zeta\omega_\mathrm{n}t\right) \sin\left(\omega_\mathrm{n}t\sqrt{1-\zeta^2} + \arccos\left(\zeta\right)\right)\right)^2. \end{aligned} \tag{4.15}$$

By comparing the power transient response with and without the second-order term in Fig. 4.6, it can be noticed that the attenuation of the second-order term $\exp(-2\zeta\omega_\mathrm{n}t)$ is relatively fast compared to the term $\exp(-\zeta\omega_\mathrm{n}t)$. The difference is noticeable by observing the power overshoot during the first full period, but after the second order term is attenuated the power transient can be approximated with only the first only term.

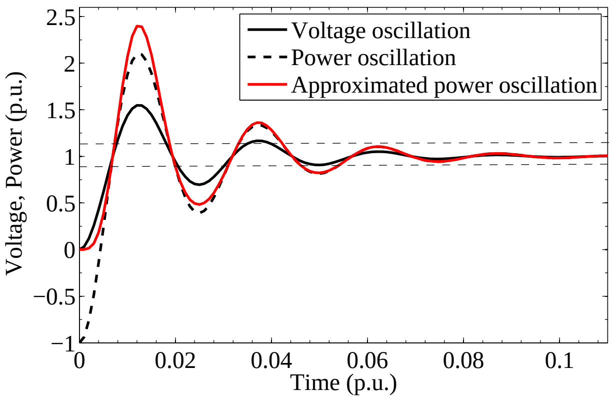

Figure 4.6: Step response of voltage (solid black line), power (dashed line) and approximated power (solid red line) relative to the steady-state value.

Finally, the settling time T_ε can be calculated from (4.15), which ensures that oscillation of $\hat{p}_\mathrm{pv}$ is attenuated between range $(-U_\mathrm{o}^2\Delta d^2/R_\mathrm{mpp})(1-\varepsilon)$ and $(-U_\mathrm{o}^2\Delta d^2/R_\mathrm{mpp})(1+$

ε) yielding (4.16).

$$T_\varepsilon = -\frac{1}{\zeta\omega_\mathrm{n}} \ln\left(\frac{\varepsilon}{2}\right), \tag{4.16}$$

where ε is the relative magnitude between 0 and 1 of steady-state value in time period T_ε. It is worth noting that the power settling time differs from voltage, which is $T_\varepsilon = -1/\zeta\omega_\mathrm{n} \ln(\varepsilon)$. Comparing these two values, it can be noticed that power has approximately 30 % higher settling time, when considering the period, where both quantities are attenuated to 10 % of their steady-state value.

It can be concluded from (4.16), that settling time is directly proportional to the PV dynamic resistance. Such behavior is demonstrated in Fig. 4.7, where the power transient response is simulated with irradiance levels $G = 1000\,\mathrm{W/m^2}$ and $G = 50\,\mathrm{W/m^2}$ for the boost-converter.

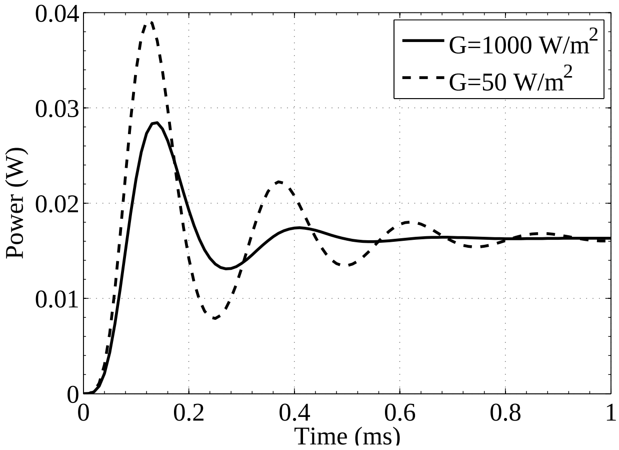

Figure 4.7: Transient step response for power after the perturbation step $\Delta d = 0.006$ is performed.

The phenomenon can be justified by observing the source admittance. When the resistance is high, meaning that source admittance $Y_\mathrm{S} = 1/r_\mathrm{pv}$ is low, the source is considered nearly ideal and any damping does not exists. Such a condition occurs in lowest irradiance level, where the static PV resistance $U_\mathrm{pv}/I_\mathrm{pv}$ is the highest.

When considering the effect of parasitics, $G^\mathrm{S}_\mathrm{ci-o}$ can be much more complex with third or higher-order transfer functions thus (4.11) and (4.13) cannot be directly used. However, it is always possible to evaluate settling time T_ε numerically by using calculation software such as Matlab$^\mathrm{TM}$. Considering the discussed boost converter with damping network added at its input, source-affeted control-to-input transfer function $G^\mathrm{S}_\mathrm{ci-o}$ has a third order dynamics. Therefore, the damping ratio is calculated numerically, which yields $\zeta = 0.186$ and natural frequency $\omega_\mathrm{n} = 2577\,\mathrm{rad/s}$. The time where input voltage u_pv and power p_pv oscillation are settled within 10 % of their final values are 0.48 ms and 0.63 ms, respectively. Since, the power oscillation needs to be settled in all circumstances before the next MPPT period, finally 0.65 ms is selected as the sampling time for later simulations.

Steady-state three-point operation of perturbative algorithms generates harmonic frequencies due to the step-wise operation waveform. Harmonic frequencies can be analyzed by calculating the Fourier series $F(s)$ for ideal P&O voltage waveform $f(t)$ in Fig. 4.5b, the representation in frequency domain can be obtained as follows

$$F(s) = \frac{2\Delta U_{\mathrm{pv}}}{n\pi}\left(\cos\left(\frac{n\pi}{4}\right) - \cos\left(\frac{3n\pi}{4}\right)\right)\frac{n\pi}{s^2 + (n\omega)^2} + \frac{\Delta U_{\mathrm{pv}}}{s}, \tag{4.17}$$

where

$$\omega = \frac{2\pi}{4T_{\mathrm{p}}} \tag{4.18}$$

and n = 1,3,5,7.. It can be concluded that the waveform contains odd harmonics i.e. third, fifth, seventh etc., whereas the corresponding periods are $4T_{\mathrm{p}}/3$, $4T_{\mathrm{p}}/5$, $4T_{\mathrm{p}}/7$. The magnitude spectrum of P&O steady-state voltage waveform is also depicted in Fig. 4.8, where the magnitude and frequency are presented relatively to the amplitude of fundamental frequency and chosen sampling time, respectively.

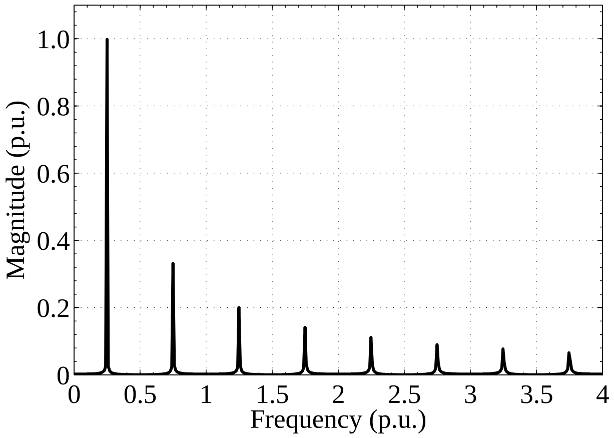

Figure 4.8: Single-sided magnitude spectrum of P&O steady-state voltage waveform relatively to the amplitude of fundamental frequency and chosen sampling time T_{p}.

If any of the harmonics occur at the natural resonant frequency of the converter, the system starts to oscillate with a limited amplitude determined by damping factor, natural angular frequency and amplitude of injected waveform. The same phenomenon is also discovered in [38] by using small-signal analysis. However, when the MPPT sampling period is selected higher than the power settling time of the system, the fundamental, first and second harmonic frequency are below the natural frequency and therefore, not affecting the dynamics of the converter. Although, the settling time is designed based on (4.16), one of the high-frequency harmonics can appear at the natural frequency of the converter. However, it is not a practical issue since the amplitude of high-frequency harmonics is very low in respect to the fundamental component.

Moreover, the step response cannot be infinitely fast in practice and therefore, the effect of high-order harmonics can be neglected.

4.2.2 Rapidly Changing Atmoshperic Conditions

The second design variable in fixed-step P&O algorithm is the perturbation step Δx. There is a compromise in selecting the value for Δx: With large value Δx, fast response can be achieved in varying atmospheric conditions, but the amplitude of oscillations are high around the steady-state operation point. In contrast, a small value reduces the oscillations around the MPP, but it makes tracker slower in varying atmospheric conditions. Moreover, MPP tracker with P&O algorithm can fail in varying irradiance conditions if the algorithm is not able to distinguish the variations of the PV power caused by the duty ratio modulation from those caused by irradiance variation. [24]

The erratic operation of perturbative algorithm can be explained by inspecting Fig. 4.9a, where the present operation point is at point A and the sign of next perturbation step is leftwards i.e. lower voltage level. If irradiance is increasing within the MPPT sampling period, the new operation point moves from A to C instead from A to B. However, this is not an issue since the power change caused by perturbation is larger than the power change caused by irradiance change corresponding to $P_{\text{pv}}(k+1) - P_{\text{pv}}(k) < 0$. Therefore, the sign of next perturbation is inversed i.e. voltage is increased and operation point converges towards MPP. In contrast, the false operation in changing irradiance condition is illustrated in Fig. 4.9b. The starting point is the same as in Fig. 4.9a, the operation point is located at point A and the sign of next perturbation is leftwards. Due to changing irradiance level between sampling periods, the operation point is moved from A to C. In this case, the sign of the next perturbation is calculated as $P_{\text{pv}}(k+1) - P_{\text{pv}}(k) > 0$ and the direction of next perturbation is leftward indicating wrong operation of the MPPT algorithm.

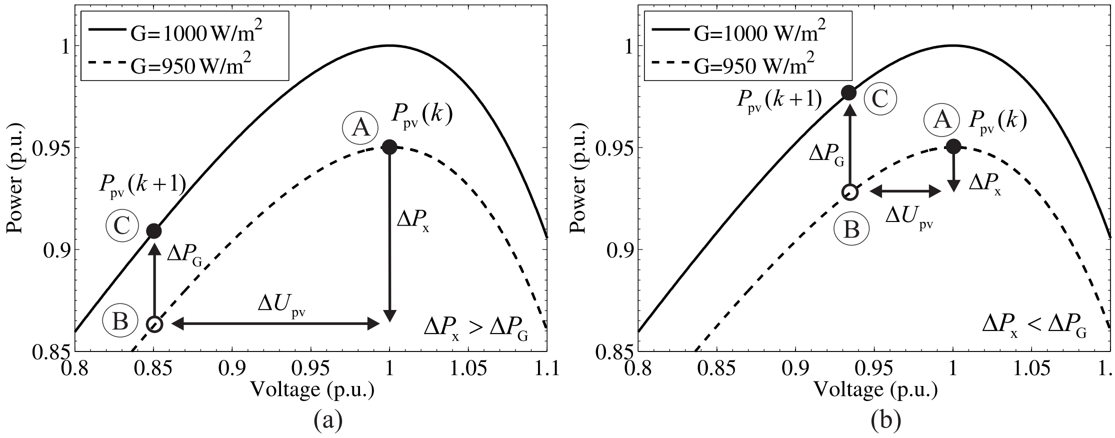

(a) (b)

Figure 4.9: Demonstration of (a) proper operation and (b) false operation of perturbative algorithms in fast-changing irradiance condition.

Basically, there are two ways to avoid such failure: First is to select the perturbation step Δx so that power variation caused by perturbation is larger than the power change caused by irradiance change. The second one is based on the additional power sample to estimate the right direction. This section discusses the optimization of perturbation step so that the maximum efficiency is achieved. In contrast, discussion about the effect of additional power sample is discussed in Section 4.2.5.

From Fig. 4.9, it can be concluded that the power variation ΔP_{x} caused by perturbation must be larger than the power variation caused by irradiance change ΔP_{G} i.e., the inequality (4.19) must be satisfied in varying atmospheric conditions.

$$|\Delta P_{\mathrm{x}}| \geq |\Delta P_{\mathrm{G}}| \,. \tag{4.19}$$

The absolute value of both power variations are used due to the fact that the sign of power variation cannot be predicted. By using absolute values, the maximum power variation is taken into account.

According to Fig. 4.9, the voltage and current variations are referred to ΔU_{pv} and ΔI_{pv}, respectively. Moreover, the power variation between k-th and $(k+1)$-th sampling instants is defined as $\Delta P_{\mathrm{pv}} = P_{\mathrm{pv}}(k+1) - P_{\mathrm{pv}}(k)$. Therefore, the power variation of two consecutive power measurements can be represented as

$$\Delta P_{\mathrm{pv}} = U_{\mathrm{mpp}} \Delta I_{\mathrm{pv}} + I_{\mathrm{mpp}} \Delta U_{\mathrm{pv}} + \Delta U_{\mathrm{pv}} \Delta I_{\mathrm{pv}}. \tag{4.20}$$

Since, ΔU_{pv} obtain large values, ΔI_{pv} cannot be evaluated with a linear relation formula. The problem is solved in [24] by using the Taylor series approximation, which has assumed to be sufficiently accurate. Main idea in Taylor series is to approximate a function as an infinite sum of terms that are calculated from the values of the function's derivatives at the single point according to the following expansion of a real function

$$f(x) = f(a) + f(a)(x-a) + \frac{f''}{2!}(x-a)^2 + ... + \frac{f^{(n)}}{n!}(x-a)^n. \tag{4.21}$$

The order n of the series determines the accuracy of approximation, which the method can produce for a function $f(x)$. The higher-order series gives more accurate approximation, but the complexity increases due to high-order derivatives need to be calculated. In [24], the authors have chosen the second-order Taylor approximation to be reasonably accurate for analysis.

PVG current is a function of voltage, irradiance and temperature as concluded in Chapter 2. By using the second-order Taylor approximation for ΔI_{pv}, the following expression can be obtained

$$\Delta I_{\mathrm{pv}} = \frac{\partial i_{\mathrm{pv}}}{\partial u_{\mathrm{pv}}}\Delta U_{\mathrm{pv}} + \frac{1}{2}\frac{\partial^2 i_{\mathrm{pv}}}{\partial^2 u_{\mathrm{pv}}}\Delta U_{\mathrm{pv}}^2 + \frac{\partial i_{\mathrm{pv}}}{\partial G}\Delta G + \frac{1}{2}\frac{\partial^2 i_{\mathrm{pv}}}{\partial^2 G}\Delta G^2 + \frac{\partial i_{\mathrm{pv}}}{\partial T}\Delta T + \frac{1}{2}\frac{\partial^2 i_{\mathrm{pv}}}{\partial^2 T}\Delta T^2. \tag{4.22}$$

Due to relatively short interval between perturbations, temperature can be assumed constant and therefore, second order variation of ΔT can be also neglected. Moreover, i_{pv} and G has a linear proportionality as shown in (2.4) and therefore second order term of G can be also ignored. With these assumptions, the ΔI_{pv} can be expressed near the MPP by using (4.23).

$$\Delta I_{\mathrm{pv}} \approx \left.\frac{\partial i_{\mathrm{pv}}}{\partial u_{\mathrm{pv}}}\right|_{\mathrm{MPP}}\Delta U_{\mathrm{pv}} + \frac{1}{2}\left.\frac{\partial^2 i_{\mathrm{pv}}}{\partial^2 u_{\mathrm{pv}}}\right|_{\mathrm{MPP}}\Delta U_{\mathrm{pv}}^2 + \left.\frac{\partial i_{\mathrm{pv}}}{\partial G}\right|_{\mathrm{MPP}}\Delta G + \left.\frac{\partial i_{\mathrm{pv}}}{\partial T}\right|_{\mathrm{MPP}}\Delta T. \tag{4.23}$$

Next step is to separate the current variation component, which is caused by perturbing the voltage and the other component which is caused by irradiance change. By using (4.23) and $U_{\mathrm{mpp}} = R_{\mathrm{mpp}} I_{\mathrm{mpp}}$, the second partial derivative of i_{pv} can be evaluated as follows

$$\frac{\partial^2 i_{\mathrm{pv}}}{\partial^2 u_{\mathrm{pv}}} = \frac{1}{N_{\mathrm{s}} akT/q}\left(1 - \frac{r_{\mathrm{s}}}{R_{\mathrm{mpp}}}\right)^3 \left(\frac{i_0}{N_{\mathrm{s}} akT/q}\exp\left(\frac{U_{\mathrm{mpp}} + r_{\mathrm{s}} I_{\mathrm{mpp}}}{N_{\mathrm{s}} akT/q}\right)\right). \tag{4.24}$$

For the simpler representation, (4.24) is marked as $(1/2)(\partial^2 i_{\mathrm{pv}}/\partial^2 2u_{\mathrm{pv}}) = -H$. Since the series resistance is relatively low compared to the parallel resistance, short-circuit current can be approximated to be the same as the photocurrent of the PVG (i.e. $i_{\mathrm{sc}} \approx i_{\mathrm{ph}}$). Partial derivative $\partial i_{\mathrm{pv}}/\partial G$ can be, therefore, approximated with material constant K_{ph} [24] as given in (4.25).

$$\frac{\partial i_{\mathrm{pv}}}{\partial G} \approx \frac{\partial i_{\mathrm{ph}}}{\partial G} = K_{\mathrm{ph}}, \tag{4.25}$$

Finally, the PVG current variation ΔI_{pv} can be expressed as a function of two terms

$$\Delta I_{\mathrm{pv}} \approx \underbrace{\frac{\Delta U_{\mathrm{pv}}}{R_{\mathrm{mpp}}} - H\Delta U_{\mathrm{pv}}^2}_{\Delta I_{\mathrm{x}}} + \underbrace{K_{\mathrm{ph}}\Delta G}_{\Delta I_{\mathrm{G}}}, \tag{4.26}$$

where ΔI_{x} and ΔI_{G} represent the current change due to the perturbation and irradiance, respectively. Now, the power variation caused by perturbation ΔP_{x} can be calculated on the basis of equations (4.20), (4.26) and $U_{\mathrm{mpp}} = R_{\mathrm{mpp}} I_{\mathrm{mpp}}$ and it can be represented as follows

$$\Delta P_{\mathrm{x}} = \Delta U_{\mathrm{x}} \Delta I_{\mathrm{x}} \approx \left(U_{\mathrm{mpp}} H + \frac{1}{R_{\mathrm{mpp}}} \right) \Delta U_{\mathrm{x}}^2, \tag{4.27}$$

where ΔU_{x} is voltage change in PVG output caused by the duty ratio or voltage reference perturbation. The power change as a function of perturbation step size relative to the STC values is illustrated in Fig. 4.10, which is based on power variation calculated with (4.27) and PVG simulation model at $G = 100\,\mathrm{W/m^2}$. The accuracy of power variation ΔP_{x} is more important at low irradiance levels, where the power variation due the perturbation is the lowest. In the simulation, both directions of perturbation are considered i.e., $\Delta P(U_{\mathrm{mpp}} + \Delta U)$ is the power change when the voltage is increased by the small perturbation step ΔU from MPP voltage. On the contrary, $\Delta P(U_{\mathrm{mpp}} + \Delta U)$ refers to the power change caused by reducing the voltage from MPP. It can be noticed from Fig. 4.10, that (4.27) gives a good approximation of power change by averaging the power change of $\Delta P(U_{\mathrm{mpp}} + \Delta U)$ and $\Delta P(U_{\mathrm{mpp}} + \Delta U)$. Since the P-U curve is not truly parabolic, current decreases more in respect to voltage in the CV region than in the CC region yielding higher power change in CV region.

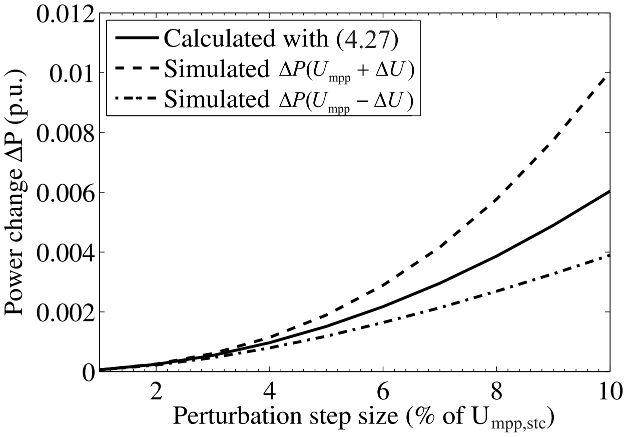

Figure 4.10: Calculated and simulated power variations for NAPS NP190Gkg PV module under $100\,\mathrm{W/m^2}$ relatively to STC quantities.

Due to the fact that the voltage variation caused by small irradiance variation can be omitted around the MPP, the power variation ΔP_{G} caused by irradiance change ΔG can be derived by multiplying MPP voltage with current variation ΔI_{G} yielding

$$\Delta P_{\mathrm{G}} \approx U_{\mathrm{mpp}} \Delta I_{\mathrm{G}} \approx U_{\mathrm{mpp}} K_{\mathrm{ph}} \Delta G. \tag{4.28}$$

It is worth noting that at low irradiance levels MPP voltage does not stay constant while irradiance changes as concluded in Chapter 2. This means that Eq. (4.28) slightly underestimates the power variation at low irradiance levels. However, taking the voltage variation into account, Eq. (4.28) would lead too complex representation for general usage. Finally, the minimum step sizes can be calculated from observation that power variations caused by perturbation need to be higher than the power variation caused by irradiance variations. This yields (4.29) and (4.30), which give a minimum perturbation step size for duty ratio Δd and input voltage reference $\Delta u_{\mathrm{in}}^{\mathrm{ref}}$ in respect to irradiance slope $\dot{G}$ within sampling period T_{p}.

$$\Delta d \geq \frac{1}{\left|G_{\mathrm{ci-o}}(s=0)\right|}\sqrt{\frac{U_{\mathrm{mpp}}K_{\mathrm{ph}}\left|\dot{G}\right|T_{\mathrm{p}}}{U_{\mathrm{mpp}}H + 1/R_{\mathrm{mpp}}}} \tag{4.29}$$

$$\Delta u_{\mathrm{in}}^{\mathrm{ref}} \geq \sqrt{\frac{U_{\mathrm{mpp}}K_{\mathrm{ph}}\left|\dot{G}\right|T_{\mathrm{p}}}{U_{\mathrm{mpp}}H + 1/R_{\mathrm{mpp}}}} \tag{4.30}$$

The standard EN 50530, which is discussed in Section 4.2.4 in more detail, defines an irradiance ramp ranging from 0.5 W/m^{2}s to 100 W/m^{2}s. The worst condition as MPPT point of view is the highest rate of change in irradiance, where the power variation is the highest. In contrast, in low irradiance levels the power variation caused by perturbation is the lowest. Therefore, the corresponding values for rate of change and irradiance level were chosen to be $\dot{G} = 100\,\mathrm{W/m^2s}$ and $G = 100\,\mathrm{W/m^2}$ to demonstrate drift phenomenon by simulations. Simulation results can be seen in Fig. 4.11, where the optimal perturbation step value $\Delta d = 0.006$ and a too low perturbation step $\Delta d = 0.001$ are superimposed in the same figure.

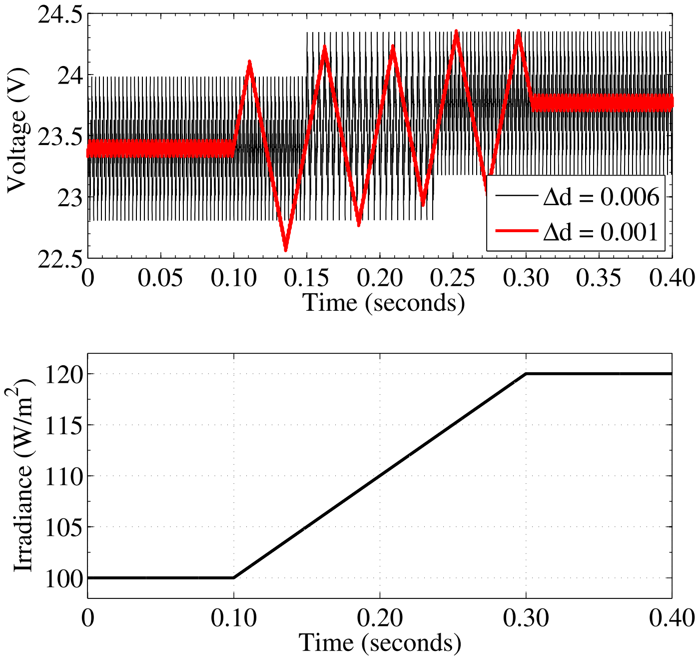

Figure 4.11: The simulated PVG voltage waveform under irradiance ramp by using two different perturbation step values.

Fig. 4.11 shows that, when the step size of perturbation is chosen properly respect to the irradiance variation, the duty ratio oscillation assumes three different values. In contrast, too low perturbation step causes the PVG voltage to drift in both sides of the MPP. The characteristic of the drift is dependent on the difference between the chosen and optimal perturbation step. If the step is chosen just a bit lower than the optimal value, the algorithm operates with one additional duty ratio value since the additional step produces the large enough power variation respect to the irradiance variation to change the sign of the perturbation. However, if the perturbation step size is relatively small respect to the optimal value, as in Fig. 4.11, the duty ratio drift up or down until the high enough power change is generated. If such a condition does not exit, the duty ratio tends to drift to upper or lower limit of controller yielding reduced energy yield.

4.2.3 Preventing the Effects of Output Voltage Fluctuation

It was assumed in the previous sections that the load of the converter is ideal or working as stand-alone operation mode. In grid-connected single-phase systems, however, the output power of inverter fluctuates at twice the grid frequency. The origin of fluctuations is sinusoidal current fed into the grid by the inverter. Since the voltage is also naturally sinusoidal, the instantaneous power fed into the grid follows the squared sinusoidal form given in (4.31).

$$p_{\mathrm{ac}} = u_{\mathrm{ac}} i_{\mathrm{ac}} = U\sin(\omega_{\mathrm{s}}t) I \sin(\omega_{\mathrm{s}}t) = UI\sin^2(\omega_{\mathrm{s}}t) = \frac{UI}{2}(1-\cos(2\omega_{\mathrm{s}}t)). \qquad (4.31)$$

This produces voltage ripple at the input voltage of the inverter, which is also twice the grid frequency. In this thesis, 50 Hz grid frequency is used yielding to 100 Hz voltage fluctuation in single-phase systems. In three-phase systems, the corresponding frequency is six times higher than the grid frequency i.e. 300 Hz. When the DC-DC converter is connected to the input of singe-phase inverter, power fluctuation can end up to the input side of the DC-DC converter. That will fluctuate the voltage of PV module reducing the energy yield and disturbing the operation of MPPT algorithms [9]. To estimate the reduction of the PV module power output due to the input voltage ripple of the converter, some simple formulas have been presented, e.g. in [39] based on the panel characteristics, and the root mean square value of ripple voltage.

The simplest way to prevent the fluctuation is to increase input capacitance for each converter. Such method, however, increases the system cost and lowers the system reliability due to the fact that the electrolytic capacitors need to be used. In contrast, the efficient way to eliminate the PV module voltage fluctuation is to implement an input-voltage control with a high enough bandwidth to attenuate the fluctuation.

In case of open-loop controlled converter, the effect of power fluctuation in respect to the input voltage variation can be analyzed by observing output-to-input transfer function $T_{\mathrm{oi-o}}$, which describes the relation between input and output voltage of the converter. If the value of $T_{\mathrm{oi-o}}$ is lower than unity, the converter is able to prevent output voltage ripple from affecting to the input voltage. The more accurate analysis can be performed for input voltage variation when the output voltage fluctuation with amplitude of ΔU_o is taken into account as in (4.32).

$$\Delta U_\mathrm{pv} = \underbrace{|G_\mathrm{ci-o}(s=0)\Delta x|}_{\Delta U_\mathrm{x}} + \underbrace{|T_\mathrm{oi-o}(s)\Delta U_\mathrm{o}|}_{\Delta U_{\Delta\mathrm{u_o}}}, \tag{4.32}$$

where ΔU_x and $\Delta U_{\Delta\mathrm{u_o}}$ are voltage variation in the PVG caused by perturbation and output voltage fluctuation, respectively. The absolute value of both term need to be taken into account, since the maximum input voltage variation is considered. Since the output voltage fluctuation is summed to the input voltage, it can be noticed in (4.27) that the voltage step caused by the perturbation need to be higher than the effect of the output voltage fluctuation to input voltage. Therefore, voltage change $\Delta U_{\mathrm{pv},\Delta\mathrm{u_o}}$ is just added to the minimum perturbation step yielding following inequality for perturbation step [40]

$$\Delta d > \frac{1}{|G_\mathrm{ci-o}(s=0)|}\sqrt{\frac{U_\mathrm{mpp}K_\mathrm{ph}\left|\dot{G}\right|T_\mathrm{p}}{U_\mathrm{mpp}H + 1/R_\mathrm{mpp}}} + \frac{|T_\mathrm{oi-o}|}{|G_\mathrm{ci-o}(s=0)|}\Delta U_\mathrm{o}, \tag{4.33}$$

where the first and the second term correspond the perturbation step needed to compensate irradiance variation and output voltage fluctuation, respectively. Since output voltage fluctuation is not related to the irradiance variation, the perturbation step is needed to be higher than the second term in (4.33) also in constant atmospheric conditions.

The more intelligent way to prevent the effect of output voltage fluctuation in comparison with increasing input capacitance is to implement converter with input-voltage control. Wide-bandwidth feedback control can reduce the voltage disturbances seen by PVG, which are generated at the converter output. Moreover, faster step response can be achieved yielding to the higher MPPT sampling frequency and smaller perturbations step sizes increasing the MPPT efficiency. In following, the effects of feedback-compensated system to the perturbative MPPT algorithms are analyzed.

The effect of output voltage fluctuation to PVG voltage under feedback control can be analyzed by observing the closed-loop reverse voltage transfer function $T_\mathrm{oi-c}$ as introduced in Chapter 3.

$$T_\mathrm{oi-c} = \frac{\hat{u}_\mathrm{in}}{\hat{u}_\mathrm{o}} = \frac{T_\mathrm{oi-o}}{1 - L_\mathrm{in}} \tag{4.34}$$

Typically, the control loop is designed to have a high gain at low frequencies to eliminate the steady-state error. This can be achieved by using a controller with an integrator resulting, theoretically, infinite gain at low frequencies. Therefore, the reference-to-input transfer function can approximated with DC gain at low frequencies, i.e, the input voltage reference matches the actual input voltage.

$$G_{\mathrm{ri}} = \frac{\hat{u}_{\mathrm{in}}}{\hat{u}_{\mathrm{in}}^{\mathrm{ref}}} = -\frac{1}{G_{\mathrm{se-u}}^{\mathrm{in}}} \frac{L_{\mathrm{in}}}{1 - L_{\mathrm{in}}} \approx \frac{1}{G_{\mathrm{se-u}}^{\mathrm{in}}} \tag{4.35}$$

To ensure proper P&O operation under the stationary atmospheric conditions, voltage variation caused by perturbation need to be larger than the voltage change caused by the output fluctuation i.e.

$$\Delta u_{\mathrm{in}}^{\mathrm{ref}} \geq \left| \frac{T_{\mathrm{oi-o}}}{1 - L_{\mathrm{in}}} \Delta U_{\mathrm{o}} \right| \tag{4.36}$$

The absolute values of terms need to be used in analysis due to the fact that the highest variation in u_{pv} need to be taken into account. Finally, the proper operation can be ensured when both irradiance variation and output voltage fluctuation are both taken into account yielding [40]

$$\Delta \hat{u}_{\mathrm{in}}^{\mathrm{ref}} \geq G_{\mathrm{se-u}}^{\mathrm{in}} \sqrt{\frac{U_{\mathrm{mpp}} K_{\mathrm{ph}} \left| \dot{G} \right| T_{\mathrm{p}}}{U_{\mathrm{mpp}} H + 1/R_{\mathrm{mpp}}}} + G_{\mathrm{se-u}}^{\mathrm{in}} \left| \frac{T_{\mathrm{oi-o}}}{1 - L_{\mathrm{in}}} \right| \Delta U_{\mathrm{o}}. \tag{4.37}$$

It can be noticed from (4.37), that the output voltage fluctuation can be prevented by modifying the controller transfer function G_{c} included in the loop gain L_{in}. Therefore, the closed-loop reverse voltage transfer function need to designed so that the attenuation at 100 Hz is as high as possible. In addition, a system needs to be stable in all conditions. For the stable system, the roots of the characteristic polynomial $1 - L_{\mathrm{in}}(s)$ must be located in the open left-half plane of the complex plane. The study of location of the roots of the characteristic polynomial can be made by observing the frequency response of the loop gain. In practice, this is done with polar and Bode plots, which are constructed by plotting the magnitude $|G(j\omega)|$ in decibels (dB) and the phase $\angle G(j\omega)$ in degrees with respect to logarithmic frequency scale. The robustness of the stability is typically related to gain (GM) and phase (PM) margins, which are related to the Bode's stability conditions. The gain margin is defined $1/\left|L_{\mathrm{in}}(s)\right|$ at the frequency, where $\angle L_{\mathrm{in}}(s) = 180^\circ$ and phase margin is $\angle L_{\mathrm{in}}(s) + 180^\circ$ at the frequency where $|L_{\mathrm{in}}(s)| = 1$. For minimum requirements for stability, gain margin of 6 dB and phase margin of 30° are typically considered.

A proportional-integral-derivative (PID) compensator was selected as a controller, which can be represented as following transfer function

$$G_{\mathrm{c}} = \frac{K_{\mathrm{in}}(1 + s/\omega_{\mathrm{z1}})(1 + s/\omega_{\mathrm{z2}})}{s(1 + s/\omega_{\mathrm{p1}})(1 + s/\omega_{\mathrm{p2}})}, \tag{4.38}$$

where K_{in} is the gain factor, ω_{z1}, ω_{z2} are the zeros and ω_{p1}, ω_{p2} are the poles of the controller. Based on the converter parameters, the both zeros were selected at 3500 Hz and the both poles at 40 kHz. Furthermore, the gain factor was selected to 700. Now Bode plots of input voltage loop gain and closed-loop reverse voltage transfer function can be plotted and it is shown in Fig. 4.12a and Fig. 4.12b, respectively.

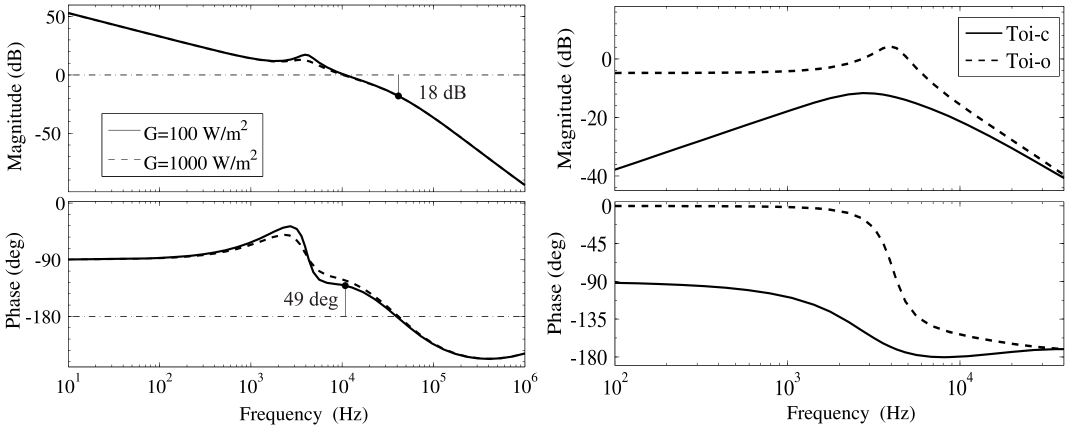

(a) (b)

Figure 4.12: Bode plots of (a) input voltage loop gain at irradiances $G = 100\,\mathrm{W/m^2}$ and $G = 1000\,\mathrm{W/m^2}$ and (b) open-loop and closed-loop reverse transfer fucntions evaluated at irradiance level $100\,\mathrm{W/m^2}$

It can be concluded from the Bode plots that the system has 4 kHz bandwidth and the gain and phase margins are 18 dB and 49 dB, respectively. Moreover, the attenuation of reverse voltage transfer function at 100 Hz are 5 dB and 38 dB for open-loop and closed-loop systems, respectively. In the other words, the closed-loop system is able to attenuate the amplitude of sinusoidal voltage output signal to 1.26 % from the original values, whereas the corresponding value for open-loop is only 56.2 %. To demonstrate the advantages of feedback controlled system in respect to the prevention of output voltage fluctuations, the open-loop and closed-loop system are compared in situation, where the output voltage is oscillating at the amplitude of 2 V. The MPPT sampling time in both systems is selected to be 1000 Hz, which ensures that the power reaches its steady-state value before the next perturbation. Moreover, the perturbation step size is selected to 0.245 V, which corresponds to the duty ratio change $\Delta d = 0.006$ in the open-loop system. The simulated operation of both systems at constant irradiance $G = 100\,\mathrm{W/m^2}$ can be seen in Fig. 4.13a.

In Fig. 4.13a, the MPPT in closed-loop system works properly, since the output voltage ripple is attenuated to $0.0126 \cdot 2\mathrm{V} = 0.0252\,\mathrm{V}$ which is lower than the voltage variation caused by perturbation. However, in the open-loop system, the amplitude of voltage ripple component is attenuated to $0.562 \cdot 2\mathrm{V} = 1.124\,\mathrm{V}$ and therefore, the perturbative step is too low to compensate the voltage fluctuation. Moreover, the incorrect power prediction of the tracker diverges the operation point from the MPP even more as can be noticed from the open-loop duty ratio waveform in Fig. 4.13b, where the increasing duty ratio correspond the decrease in input voltage. It is worth noting that in this case it is not recommended to increase the perturbation step to

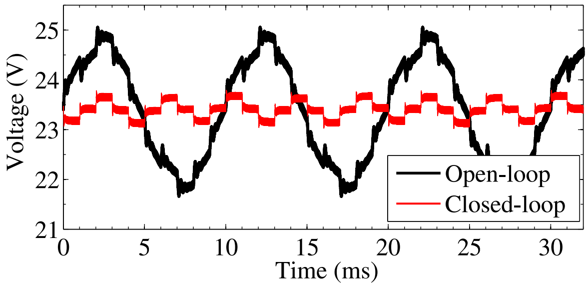

(a)

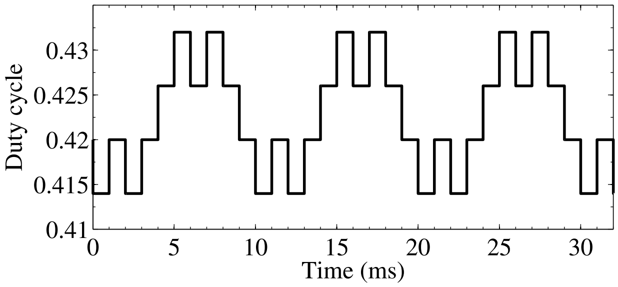

(b)

Figure 4.13: The simulated open-loop and closed-loop system under output voltage fluctuation. The figure (a) represents voltage waveforms of both system and (b) the duty ratio waveform generated by MPPT algorithm in case of open-loop system.

overcome the voltage fluctuation in open-loop system since the operation would deviate too much from the MPP thus reducing energy yield significantly.

An another advantage of feedback control over the open-loop system is the faster step response and therefore, faster sampling time of the perturbative algorithms can be used. The advantage of fast step response of the closed-loop converter is illustrated in Fig. 4.14, which compares the transient step responses of open-loop and closed-loop system.

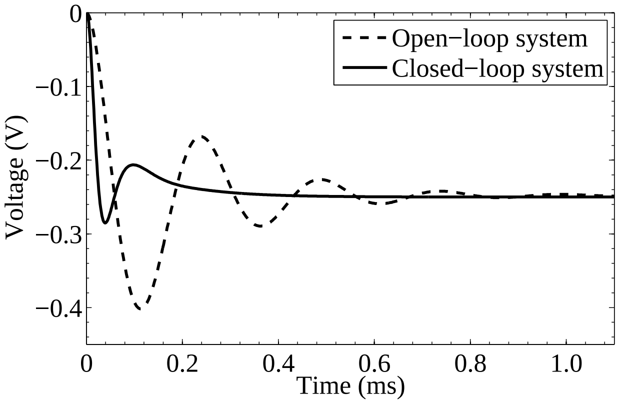

Figure 4.14: Step responses of the open-loop (dashed line) and closed-loop (solid line) systems for low irradiance $G = 100\,\mathrm{W/m^2}$

The voltage settling time in closed-loop system is 2.6 times faster than the corresponding open-loop system. Due to the fact that the sampling time in perturbative algorithms can be shorter, the perturbation step size can be reduced yielding to higher steady-state MPPT efficiency. The P&O method sampling time under feedback control can be obtained by analyzing the input voltage loop gain. Basically, the system settling time is related to the loop gain crossover frequency, where the higher gain yield faster time response. The power settling time can be analyzed by means of similar procedure as in open-loop system i.e. analyzing the behavior $\hat{p}_{\mathrm{pv}} = -\hat{u}_{\mathrm{pv}}^2/R_{\mathrm{mpp}}$. However, the reference-to-input voltage is high-order transfer function and therefore, settling time need be evaluated numerically by using e.g. Matlab$^{\mathrm{TM}}$.

4.2.4 Steady-State and Dynamic Efficiency

The important factor to benchmark different MPPT algorithm is the MPPT efficiency, which defines the ratio between actual energy and maximum energy available from PVG. The MPPT efficiency is defined as follows

$$\eta_{\mathrm{mppt}} = \frac{\int_0^t p_{\mathrm{pv}}(t)dt}{\int_0^t p_{\mathrm{mpp}}(t)dt} = \frac{\int_0^t u_{\mathrm{pv}}(t)i_{\mathrm{pv}}(t)dt}{\int_0^t p_{\mathrm{mpp}}(t)dt}, \tag{4.39}$$

where $p_{\mathrm{pv}}(t)$ is output power of the PV simulator connected in DC-DC converter and $p_{\mathrm{mpp}}(t)$ is the MPP power. While the fixed-step P&O algorithm operates in steady-state with three operation points, MPPT period is $4T_{\mathrm{p}}$ and the efficiency can be calculated as

$$\eta_{\mathrm{mppt}} = \frac{2P_{\mathrm{mpp}} + P(U_{\mathrm{mpp}} + \Delta U_{\mathrm{pv}}) + P(U_{\mathrm{mpp}} - \Delta U_{\mathrm{pv}})}{4P_{\mathrm{mpp}}}, \tag{4.40}$$

In an optimum case, the middle operation point is located at MPP and the side ones at the same power on the ascending and descending sides of the P-U curve as illustrated in Fig. 4.15. It can be concluded from the figure that the parabolic approximation is valid especially with sufficiently low perturbation steps.

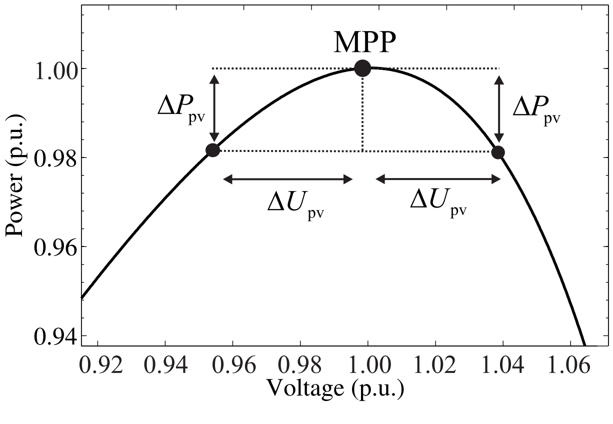

Figure 4.15: Demonstration of ideal three point operation of P&O algorithm with two different power levels.

This yields to more simplified representation for MPPT efficiency

$$\eta_{\mathrm{mppt}} = \frac{2P_{\mathrm{mpp}} + 2\left|P_{\mathrm{mpp}} - |\Delta P_{\mathrm{x}}|\right|}{4P_{\mathrm{mpp}}} = 1 - \frac{|\Delta P_{\mathrm{x}}|}{2P_{\mathrm{mpp}}} \tag{4.41}$$

$$= 1 - \frac{\left(U_{\mathrm{mpp}}H + \frac{1}{R_{\mathrm{mpp}}}\right)\Delta U_{\mathrm{x}}^2}{2P_{\mathrm{mpp}}}, \tag{4.42}$$

where ΔP_{x} and ΔU_{x} refers to power and voltage variation caused by perturbation as introduced in (4.27). However, the P-U curve of the PV cell is not truly parabolic over the MPP but rather steeper on the CV side lowering the MPPT efficiency in higher perturbation steps.

To benchmark the different MPPT techniques, a standard European efficiency EN50530 for testing DC-AC converters have been introduced. The standard defines a test procedure for the measurement of MPPT efficiency of the inverter used in grid-connected PV systems with a PV simulator in steady-state and time varying irradiance conditions. The static efficiency η_{eu} is calculated by the weighted mean of six irradiance values as follows [41]

$$\eta_{\mathrm{eu}} = 0.03\eta_{5\%} + 0.06\eta_{10\%} + 0.13\eta_{20\%} + 0.10\eta_{30\%} + 0.48\eta_{50\%} + 0.20\eta_{100\%}, \tag{4.43}$$

where $\eta_{i\%}$ is the conversion efficiency at $i\%$ of the inverter output rated power. By using (4.27), (4.42) and MPP values in Appendix A (Tab. A.2), European efficiencies can be calculated with different perturbation steps and the results can be seen in Fig. 4.16. The calculated efficiencies were also collected in Appendix A (Tab. A.3). Moreover, the same table includes European efficiencies, which were calculated with the simulation model by using different perturbation steps in irradiance levels 50, 100, 200, 300, 500 and 1000 W/m^2.

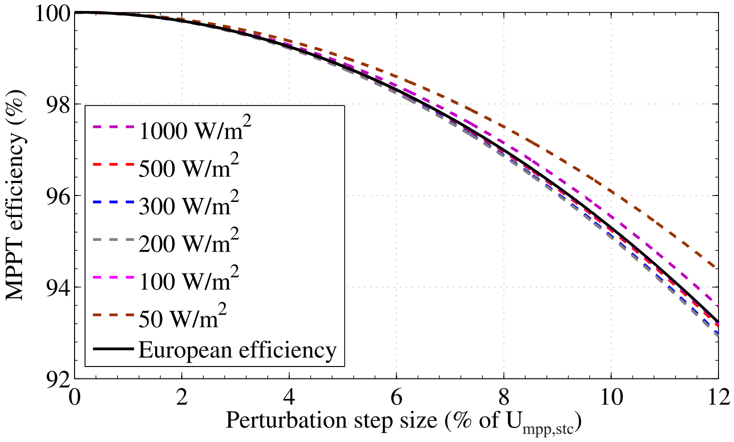

Figure 4.16: Calculated steady-state MPPT efficiency as a function of perturbation step in different irradiance levels.

Comparing the calculated and simulated efficiencies in the table, it can concluded that (4.42) produces sufficiently accurate approximation for efficiency. It can be also noticed that, when perturbation step is below 5 % of the MPP voltage, European efficiency stays higher than 99 %. To reach required 99.5 % efficiency in constant uniform atmospheric conditions for NAPS NP190GKg PV module, the perturbation step is needed to be chosen lower than 4.5 % of MPP voltage in STC.

Before European standard, there were not any guidelines available to benchmark the different MPPT algorithms in varying atmospheric conditions. Earlier, the irradiance slope 30 $\mathrm{W/m^2}$ was generally used in testing MPPT algorithm performance in dynamic conditions [42]. In the standard EN 50530, the dynamic test procedure consist of two test sequences, where the first one emulates the low irradiance variation between 10% and 50%, and the second one emulates the high irradiance variation between 30% and 100% in STC [41]. The irradiance profile is trapezoidal, where the irradiance transition is performed rising and descending ramps with 10 s dwell time between the transitions. An illustration of the dynamic test procedure can be seen in Fig. 4.17.

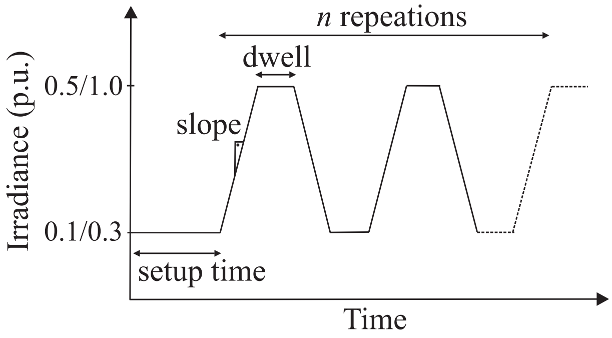

Figure 4.17: Dynamic efficiency test procedure based on the standard EN 50530.

The slopes are varying from $0.5\,\mathrm{W/m^2}$ to $50\,\mathrm{W/m^2}$ in low irradiance variation test and from $10\,\mathrm{W/m^2}$ to $100\,\mathrm{W/m^2}$ in high irradiance variation test.

The dynamic efficiency of perturbative algorithms depends on the perturbation step size and sampling time. Choosing too small combination of step and sampling time yields to drift phenomenon and reducing the MPPT efficiency, as discussed in Chapter 4. By fulfilling the inequality in (4.30), the dynamic efficiency is maximized. Considering the discussed boost converter with damping network added at its input, the source-affeted control-to-input transfer function $G^{\mathrm{S}}_{\mathrm{ci-o}}$ has third-order dynamics. Therefore, damping ratio is calculated numerically, which yields $\zeta = 0.179$ and natural frequency of $\omega_{\mathrm{n}} = 4106.2\mathrm{Hz}$. The time, where input voltage u_{pv} and power p_{pv} oscillation are settled within 10 % of final value are 0.49858 ms and 0.648679 ms, respectively. Since, the power oscillation need to be settled in all circumstance before next the MPPT period, 1540 Hz is chosen for sampling time for MPPT algorithm. The step size for the P&O algorithm is designed by using (4.29) yielding $H = 0.0105\,\mathrm{A/V^2}$ and $\Delta d = 0.006$ under low irradiance condition $G = 100\,\mathrm{W/m^2}$. Corresponding values under high irradiance condition $G = 1000\,\mathrm{W/m^2}$ are $H = 0.0865$ and $\Delta d = 0.0022$.

The simulation was also performed with too low perturbation step value, which was selected as $\Delta d = 0.0022$ The simulation result during the increasing irradiance slope can be seen in Appendix B (Fig. B.1), where the operation of both perturbation step sizes are superimposed in the same figure. When the parameters are chosen based on (4.29), the algorithm is not confused during the varying irradiance condition and the efficiency under trapezoidal test procedure is 99.97 %. In contrast, too low step size yield to drift, since the power variation caused by irradiance is too large compared to the power change caused by the perturbation. However, the algorithm is still able to perform lower oscillation around the MPP than the optimized algorithm. Therefore, the efficiency is 99.99 %. Based on the simulation, the drift phenomenon is not really an issue in perturbative algorithms, since perturbation step need to selected a lot smaller than the optimum one to saturate the controller to upper or lower limit in dynamic irradiance conditions.

4.2.5 Improvements on the Conventional Techniques

The fixed-step P&O algorithm is widely used in PV systems since it is simple and easy to implement, especially, in digital form. However, the overall MPPT performance can be further improved by modifying the traditional fixed-step P&O algorithm. The most of the introduced improvements focus on adjusting the perturbation step size in respect to the operation point on I-U curve and modifying the perturbation direction decision process, which are both discussed in this section.

Adaptive and variable-step algorithms are introduced to overcome the classical trade-off situation between the steady-state oscillation and fast dynamics in fixed-step perturbative algorithms. The conventional concept of adaptive-step algorithm is based on varying the step size of the perturbation while the sampling frequency is kept constant. As the traditional P&O algorithm, the adaptive-step perturbative algorithm can be also implemented in open-loop or closed-loop converters as illustrated in Fig. 4.18.

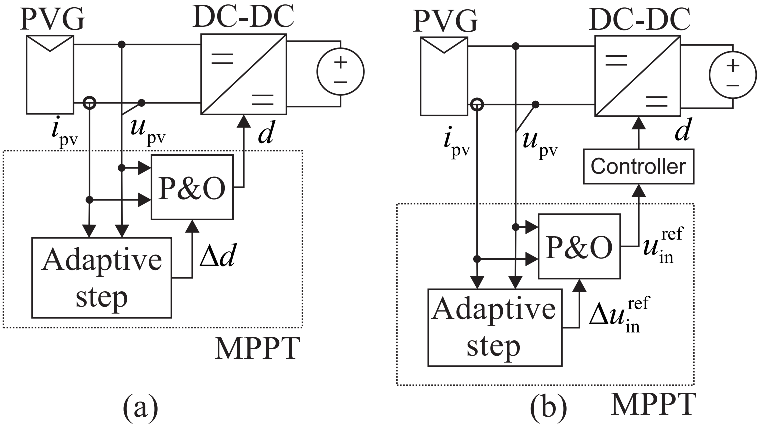

Figure 4.18: Open-loop and closed-loop control schemes with adaptive perturbative MPPT algorithms.

Basically, the algorithm adjust the step size Δx depending on how far the operation voltage is from the MPP. When the present operation point is far from MPP, large step-size is used to achieve the MPP faster. In contrary, small step-size is used when operating near the MPP to minimize steady-state oscillations. In order to calculate the value of step size, the power-voltage derivative $\Delta p_{\mathrm{pv}}/\Delta u_{\mathrm{pv}}$ is introduced as a suitable parameter for tuning the step size [43]. The P-U derivative suits well for adaptive-step purposes as can be concluded from in Fig. 4.19, which represents the correlation between P-U and the slope P-U derivative. When the operation point is located far from the MPP, the step size has a large value while it monotonically decreases when operation point is approaching the MPP.

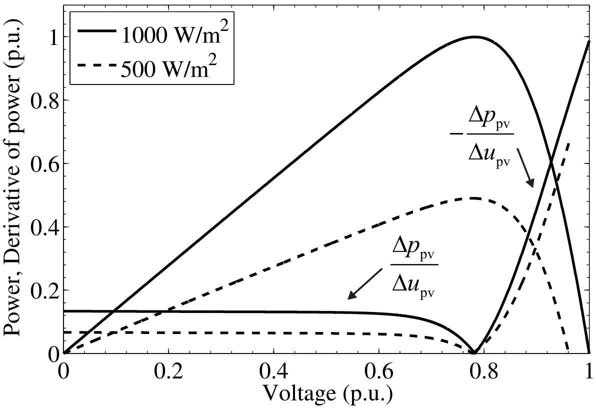

Figure 4.19: P-U curve and the absolute value of derivative of P-U curve in two different irradiance levels.

In case of an open-loop DC-DC converter, where MPP tracker controls directly the duty ratio d, the perturbation step is updated according to (4.44) [44]

$$d(k) = d(k-1) \pm N \left| \frac{\Delta P_{\mathrm{pv}}}{\Delta U_{\mathrm{pv}}} \right| = d(k-1) \pm N \left| \frac{P_{\mathrm{pv}}(k) - P_{\mathrm{pv}}(k-1)}{U_{\mathrm{pv}}(k) - U_{\mathrm{pv}}(k-1)} \right| , \tag{4.44}$$

where $d(k)$ and $d(k-1)$ are the converter duty ratio at time instants k and $k-1$, respectively. Scaling factor N is needed to adjust $|\Delta P_{\mathrm{pv}}/\Delta U_{\mathrm{pv}}|$ for a proper duty ratio level and it has a significant effect on the performance of the adaptive-step algorithm as shown in later simulations. The maximum value for N can be determined for step $|\Delta P_{\mathrm{pv}}/\Delta U_{\mathrm{pv}}|$ by following inequality

$$\Delta d_{\max} > N \left| \frac{\Delta P_{\mathrm{pv,\,max}}}{\Delta U_{\mathrm{pv,\,max}}} \right| , \tag{4.45}$$

where $\Delta d_{\max}$ is maximum desired step change. The perturbation step need to be limited to avoid too large step changes. Although any guidelines do not exit in the literature how $\Delta d_{\max}$ should be chosen, the minimum value for $\Delta d_{\max}$ can be determined similarly as done in the fixed-step P&O algorithm based on (4.29). That ensures that the adaptive-step algorithm is capable to produce large enough perturbation step to overcome the power change caused by irradiance variation. The minimum value $N_{\min}$

for scaling factor can be solved from (4.45) yielding

$$N < \frac{|\Delta U_{\mathrm{pv,max}}|\,\Delta d_{\mathrm{max}}}{|\Delta P_{\mathrm{pv,max}}|} \tag{4.46}$$

where $\Delta U_{\mathrm{pv,max}}$ and $\Delta P_{\mathrm{pv,\,max}}$ denote the maximum change of voltage and power in maximum duty ratio change Δd_{max}. If inequality in (4.46) is violated, step size saturates to the Δd_{max} and the tracker operates as fixed-step algorithm. The minimum value for scaling factor can be obtained by

$$N_{\mathrm{min}} = \min\left\{\frac{1}{(U_{\mathrm{mpp}}H + 1/R_{\mathrm{mpp}})G_{\mathrm{ci-o}}(s=0)}\right\}, \tag{4.47}$$

where $\Delta P_{\mathrm{pv,max}}$ is substituted for (4.27). The scaling factor attain its minimum value when the denominator got its maximum. Obviously, it is in maximum irradiance condition, where the $|\Delta p_{\mathrm{pv}}/\Delta u_{\mathrm{pv}}|$ is the largest. Finally, the flowchart of the adaptive perturbative algorithm is represented in Fig. 4.20.

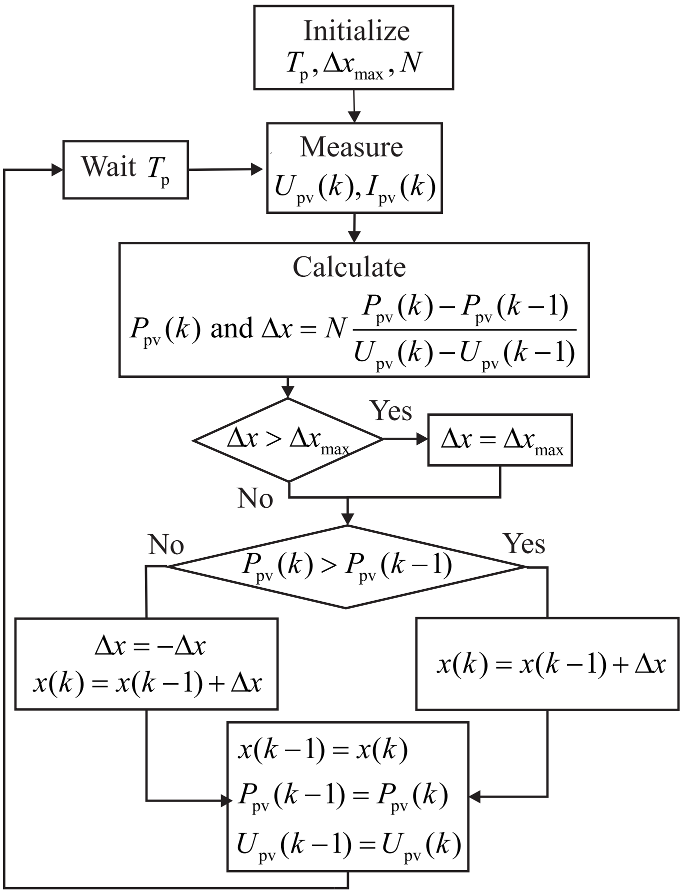

Figure 4.20: A flowchart of the adaptive-step perturbative algorithm.

To simulate operation of adaptive-step perturbative algorithm, the scaling factor N was designed at $G = 1000\,\mathrm{W/m^2}$ yielding $N = 0.0098$. Corresponding value at low irradiance $G = 100\,\mathrm{W/m^2}$ is 0.1176, which would cause fixed-step operation since inequality in (4.47) is violated. The dynamic performance of adaptive perturbative algorithm with two different scaling factor values is simulated in Fig. 4.21, where irradiance step change from $G = 100\,\mathrm{W/m^2}$ to $G = 500\,\mathrm{W/m^2}$ occurs at $t = 5\,\mathrm{ms}$. Since the $\Delta p_{\mathrm{pv}}/\Delta u_{\mathrm{pv}}$ increases while irradiance increases, the scaling factor value designed at $G = 100\,\mathrm{W/m^2}$ is too large for higher irradiance yielding to fixed-step operation. In contrast, the properly designed scaling factor, $N = 0.0098$ convergences the new MPP fast without steady-state oscillations.

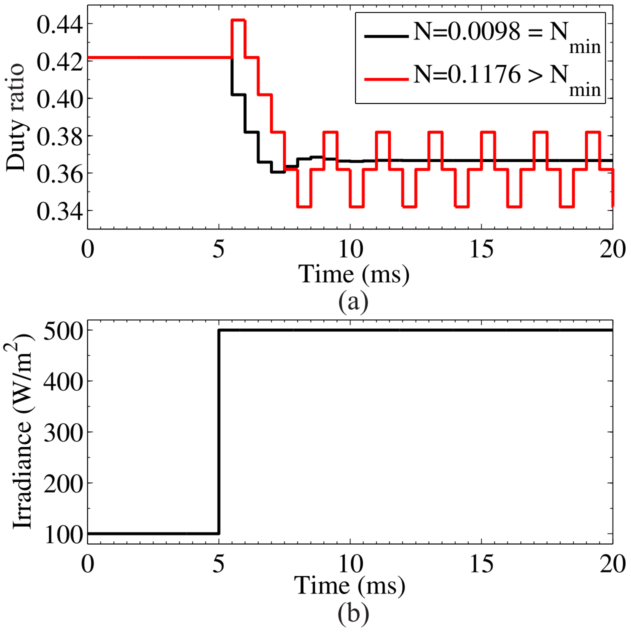

Figure 4.21: The simulated operation of adaptive-step perturbative algorithm with two different scaling factor values under irradiance step condition.

The power prediction in adaptive-step algorithms is based on the same differentiation of two consecutive power calculation from voltage and current measurements as the traditional P&O algorithm. Therefore, the same drift problem is also present in variable-step algorithms as discussed in Section 4.2.2. However, the variable-step size algorithms are more sensitive to drift, since the step size reduces around the MPP. This yields the situation where even a slight irradiance change is enough to produce power change that is higher than the power change caused by the perturbation yielding to false operation.

The valid operation of most of the presented variable-step algorithms is usually verified by using irradiance step, as in Fig. 4.21, to simulate rapidly changing irradiance condition as done in [45–47]. However, it can be seen in later simulations that using the step-wise irradiance test does not reveal the drift problem. In addition, as discussed in Chapter 2 irradiance transitions in real atmospheric conditions are always ramp-wise. The operation of adaptive-step P&O algorithm is simulated in dynamic conditions using trapezoidal irradiance profile, where irradiance changes from $G = 300\,\mathrm{W/m^2}$ to $G = 320\,\mathrm{W/m^2}$ with irradiance slope of $\dot{G} = 100\,\mathrm{W/m^2s}$. The results can be seen in Fig. 4.22, where the optimal scaling factor value and too low are compared to the fixed-step P&O operating with $\Delta d = 0.01$. The sampling time $T_{\mathrm{p}} = 1\,\mathrm{ms}$ was used in both simulations.

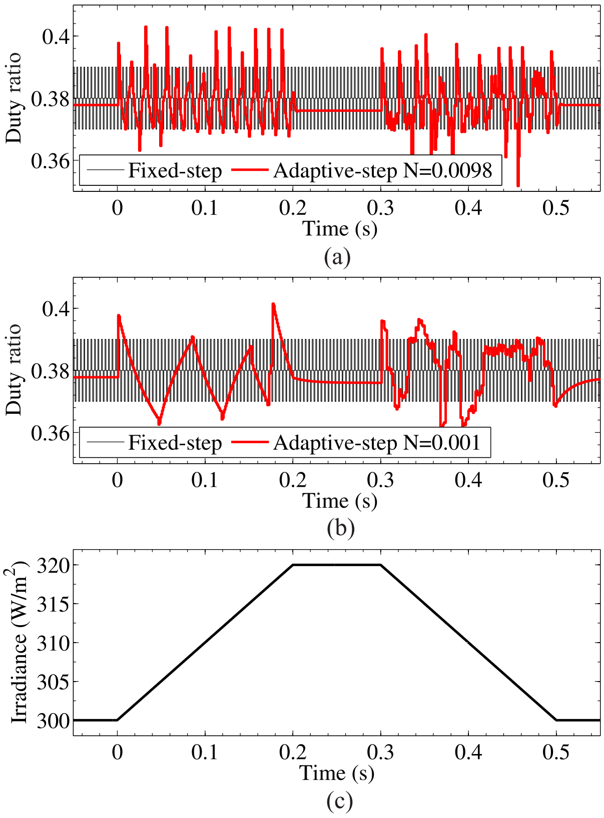

(a)

(b)

(c)

Figure 4.22: Simulated operation of adaptive-step perturbative algorithm with (a) optimized and (b) too low scaling factor value under irradiance profile (c).

Based on the simulations, adaptive-step perturbative algorithm achieve much better steady-state operation compared to the fixed-step perturbative algorithm as can be seen in Fig. 4.22a and 4.22b between the time period 0.2–0.3 s. The algorithm is able to reach the MPP without oscillatory behavior. However, in dynamic condition, the varying irradiance causes algorithm to drift on both sides of the MPP. In case of optimized scaling factor in Fig. 4.22, the algorithm causes duty ratio to oscillate around the MPP. Lowering the scaling factor does not improve the situation. In fact, the low scaling factor make system slow to track the MPP in rapidly changing environmental condition and the system convergences to the MPP slowly after wind up. This can be also observed by comparing the last 0.05 s in Figs 4.22a and 4.22b. Since the adaptive-step algorithm tends to drift easily in varying atmospheric conditions, it would wiser to divide P-U curve into several regions with individual step sizes as done in [48].

Despite the simplicity of power decision process with two consecutive power measurements, as a drawback it has been shown to fail in varying irradiance conditions. Therefore, some improvements to the basic power prediction have been developed. The drift problem can be overcome by using improved perturbative algorithm called dP-P&O. It performs an additional measurement in the middle of the MPPT sampling period, which is used to predict the direction of power. [49] With the additional power measurement, the power change caused by perturbation itself can be separated from the power change caused by the irradiance change. The operation of dP-P&O algorithm is demonstrated in Fig. 4.23, where points A,B,C and D correspond different operation points on P-U curve.

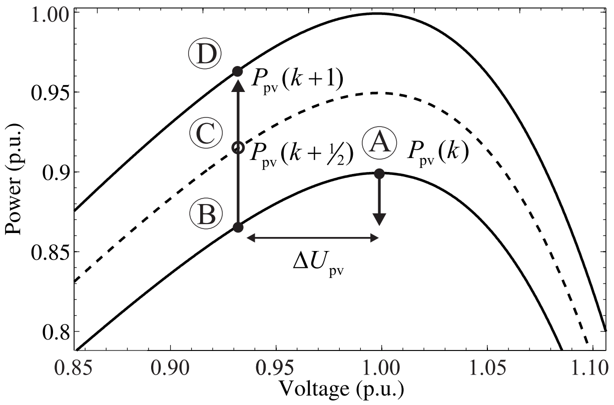

Figure 4.23: Demostration of dP-P&O algorithm operation in rapid varying irradiance condition.

Let us suppose that the system is working at k-th sampling instant at point A and the operation point moves leftwards with amount of ΔU_{pv}. If the irradiance is changing with a constant rate of speed within MPPT period, the operation point moves from A to D instead of moving from A to B. This yields to negative sign between of $P_{\mathrm{pv}}(k)$ and $P_{\mathrm{pv}}(k+1)$ and false operation of algorithm as described more detail in Section 4.2.2. However, using an additional power measurement $P_{\mathrm{pv}}(k+1/2)$ in point C, false operation of the tracker can be avoided. Assuming that power oscillation is settled in the middle of the MPPT period in $P_{\mathrm{pv}}(k+1/2)$, the power change between C and D is purely caused by irradiance change. Since the power change between points A and D within whole MPPT is measured, the power change caused by perturbation can be compared to the power change caused by the irradiance change yielding the new equation for calculating the power change given in (4.48).

$$\Delta P_{\mathrm{pv}} = 2P_{\mathrm{pv}}(k+1/2) - P_{\mathrm{pv}}(k+1) - P_{\mathrm{pv}}(k). \tag{4.48}$$

The simulated operation with and without the additional power prediction can be seen in Fig. 4.24, where irradiance changes from $G = 300\,\mathrm{W/m^2}$ to $G = 320\,\mathrm{W/m^2}$ with rate of irradiance variation of $\dot{G} = 100\,\mathrm{W/m^2}s$. The sampling time $T_{\mathrm{p}} = 1\,\mathrm{ms}$ and perturbation step $\Delta d = 0.0006$. Based on discussion in Section 4.2.2, the combination of such sampling and perturbation step is not fast enough to produce power variation which overcomes the irradiance variation. However, it can be seen in Fig. 4.24, that duty ratio follows the MPP accurately and the drift phenomenon does not exist when the additional power prediction is used. Despite the simplicity of dP-P&O algorithm, it has a drawback. Since the additional power measurement is done in the middle of MPPT period, it requires that the power oscillation must be settled down before half of the MPPT period to ensure proper voltage and current measurement. This reduces

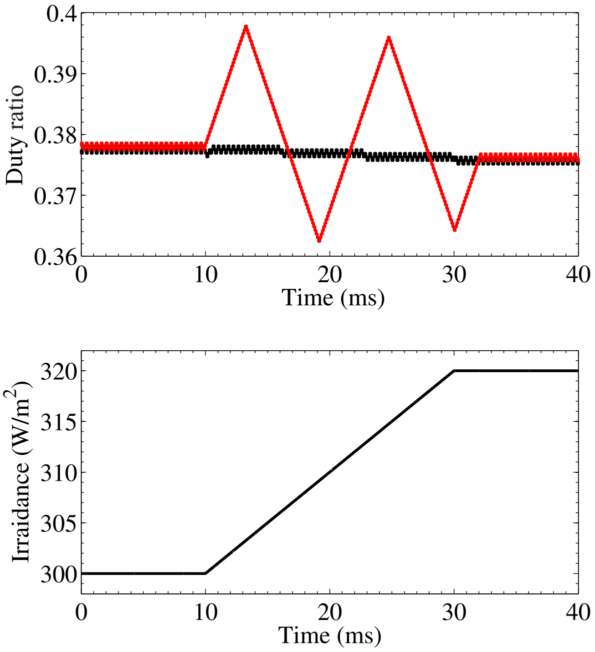

Figure 4.24: Simulated P&O algorithm operation under varying irradiance condition with (black line) and without (red line) the additional power prediction.

the maximum MPPT sampling frequency to half from the optimum value.

5. MEASUREMENTS

All measurements presented in this chapter has been made by using Agilent E4360A solar array simulator (SAS) as a source and Chroma 63103A as a voltage load. The SAS is connected to the input of boost converter, which is controlled via Texas Instruments‘ eZdsp TMS320F28335 development platform. The DSP takes voltage and current measurements, and implement the MPPT algorithm and the controller by using the C programming language. Finally, DSP generates the duty cycle for driver circuit, which controls the MOSFET. The prototype of the boost converter and the parameters are the same as used in simulations and more detailed description about the prototype can be found in [16].

Agilent E4360A can be programmed to operate in three different modes: voltage source with limited short-circuit current, current source with limited output voltage or as source emulating an actual PV generator, which was used in the measurements. Prior research in [5] have been shown that E4360A can emulate the dynamical properties of NAPS NP190Kg PV module accurately enough. In the emulating mode, the user inserts the open-circuit voltage, the short-circuit current and MPP voltage and current to SAS with control panel or serial bus via PC. It is also possible to insert multiple I-U curves whereas the transition time between each curve can be determined. The list can contain up to 512 individually programmed curves, where the minimum dwell time for each curve is 30 ms, when the 8-bit resolution is selected.

The input voltage measurement circuit consist of a differential amplifier with a low-pass filter as shown in more detail in [16]. To ensure maximum accuracy for the input current measurement, the input current is measured with Tektronix TCP312A current probe connected with TCPA300 current probe amplifier. Since the maximum output voltage of the TCPA300 is 5 V, it cannot measure the whole current range up to 8 A and therefore 10 times attenuation need to be used. The output of the current probe amplifier is scaled to between 0–3 V for the AD converter by using differential amplifier similar as used in input voltage measurement. The schematics of the input current measurement can be seen in Appendix D.

5.1 Effect of ADC Quantization Error

Since a measurement result is only an estimation of the value of the specific quantity, the deviation of a measured value to the true value need to be taken into account in applications, where accuracy of the measurements is critical. The operation of P&O algorithm is very depended on perturbation sign decision process based on two consecutive power samples and therefore, the uncertainty should be taken into account when choosing the design parameters for perturb-based algorithms. The most significant noise sources affecting MPPT process are the switching ripple noise, the measurement errors, the errors in numerical elaboration, and the output voltage noise. [20, pp. 126-138]

Due to the fact that the voltage and current measurement circuits were equipped with analog low-pass filters and samples were performed in the middle of the switching period, the effect of switching ripple noise is very minimal and it can neglected. Moreover, the prototype converter is connected to constant voltage load, thus, any output voltage fluctuation does not exit. Therefore, the uncertainty in power measurements can be approximated by analyzing the voltage and current measurement error in analog-to-digital converter of the DSP.

The sensed voltage and current values can be represented with their corresponding scaled true quantities and including the uncertainty values of voltage $\mathbf{u}_\mathrm{u}$ and current $\mathbf{u}_\mathrm{i}$ in (5.1).

$$\begin{aligned} u_\mathrm{se,in} &= G_\mathrm{se-u}^\mathrm{in} u_\mathrm{pv} \pm \mathbf{u}_\mathrm{u} \\ i_\mathrm{se,in} &= G_\mathrm{se-i}^\mathrm{in} i_\mathrm{pv} \pm \mathbf{u}_\mathrm{i} \end{aligned} \tag{5.1}$$

By applying the uncertainty propagation law to the measured power $p_\mathrm{se,in} = u_\mathrm{se,in} i_\mathrm{se,in}$, the uncertainty of power measurement by AD converter can be represented as follows [20, p. 132]

$$\mathbf{u}_\mathrm{p} = \frac{\sqrt{u_\mathrm{se,in}^2 \mathbf{u}_\mathrm{i}^2 + i_\mathrm{se,in}^2 \mathbf{u}_\mathrm{u}^2}}{G_\mathrm{se-u}^\mathrm{in} G_\mathrm{se-i}^\mathrm{in}} = \sqrt{u_\mathrm{pv}^2 \left(\frac{\mathbf{u}_\mathrm{i}}{G_\mathrm{se-i}^\mathrm{in}} \right)^2 + i_\mathrm{pv}^2 \left(\frac{\mathbf{u}_\mathrm{u}}{G_\mathrm{se-u}^\mathrm{in}} \right)^2} \tag{5.2}$$

Due to the digital implementation, the ADC has the limited number of discrete values it can produce over the range of analog values. In general, the minimum change in the voltage required to guarantee a change in the ADC output is determined by the least significant bit (LSB) voltage. This can be calculated by the full-scale output voltage and number of bits in ADC as follows

$$\mathbf{u}_\mathrm{u} = \mathbf{u}_\mathrm{i} = \frac{1}{2}\mathrm{LSB} = \frac{1}{2}\frac{U_\mathrm{fs}}{2^\mathrm{B}} \tag{5.3}$$

where U_fs refers to the full-scale voltage of the ADC and B is the amount the maximum bits. TMS320F28335 has 12 bits ADC with 3 V full-scale voltage and therefore, the resolution of the DSP is 0.366 mV. Due to the limited ADC input voltage, it is mandatory to adjust the PVG voltage and current measurements to proper level for DSP. This is done by scaling the input voltage and current measurements with scaling factors $G_\mathrm{se-u}^\mathrm{in}$ and $G_\mathrm{se-i}^\mathrm{in}$, which are defined with full-scale value and the maximum measured values as follows

$$G_{\text{se}-\text{u}}^{\text{in}} = \frac{U_{\text{fs}}}{U_{\text{pv,max}}},\ G_{\text{se}-\text{i}}^{\text{in}} = \frac{U_{\text{fs}}}{I_{\text{pv,max}}} \tag{5.4}$$

Now the effect of uncertainty measured power variation due to two consecutive power measurements can be given in (5.5).

$$\Delta P_{\text{pv},\mathbf{u}_\text{p}} = (P_{\text{pv}}(k+1) + \mathbf{u}_\text{p}) - (P_{\text{pv}}(k) + \mathbf{u}_\text{p}) = \Delta P_{\text{pv}} + 2\mathbf{u}_\text{p}, \tag{5.5}$$

where $\Delta P_{\text{pv},\mathbf{u}_\text{p}}$ is measured power variation including the uncertainty. It can be noticed that the power variation in PVG need to be larger than uncertainty term $2\mathbf{u}_\text{p}$ to ensure proper power prediction. Finally, the formula for minimum perturbation step can be obtained in varying irradiance condition by adding the uncertainty term $2\mathbf{u}_\text{p}$ to ΔP_G in (4.19) yielding

$$\Delta d \geq \frac{1}{|G_{\text{ci}-\text{o}}(s=0)|} \sqrt{\frac{U_{\text{mpp}} K_{\text{ph}} \left|\dot{G}\right| T_\text{p} + 2\sqrt{u_{\text{pv}}^2 \left(\frac{\mathbf{u}_\text{i}}{G_{\text{se}-\text{i}}^{\text{in}}}\right)^2 + i_{\text{pv}}^2 \left(\frac{\mathbf{u}_\text{u}}{G_{\text{se}-\text{u}}^{\text{in}}}\right)^2}}{U_{\text{mpp}} H + 1/R_{\text{mpp}}}}. \tag{5.6}$$

Since the minimum ADC quantization error stays constant despite of irradiance changes, the worst case in choosing minimum perturbation step is at low irradiance levels where the perturbation step yields to the smallest power variation. Using the 100 W/m^2 as a low irradiance level, Eq. (5.6) yields to $\Delta d \geq 0.0129$. It can be noticed that the value is over two times higher than the value achieved in ideal conditions. Choosing perturbation step higher than 0.0129, ensures that the quantization error of power is always smaller than the measured power variation and the MPPT algorithm can distinct the power variation caused by perturbation properly. The perturbation step corresponds to 2% of U_{mpp} yielding 99.8 % theoretical maximum steady-state efficiency, which is still excellent.

5.2 Steady-State Operation

To test MPPT operation in steady-state conditions, irradiance levels of 100 and 1000 W/m^2 were used corresponding to the low and high irradiance conditions, respectively. The measured PVG voltage and current waveforms were saved with LeCroy104MXi oscilloscope by using high sampling frequency. The data was inserted to the Matlab$^{\text{TM}}$, where the plotting and efficiency calculations were performed. The measured input voltage with the MPP voltage in maximum irradiance condition is depicted in Fig. 5.1. This corresponds to the easiest environmental condition for MPPT algorithm, since the power variation caused by the perturbation is the largest and irradiance is constant. It can be seen that the MPPT algorithm works properly with three operation points, one close to the MPP and one in CC region and CV region.

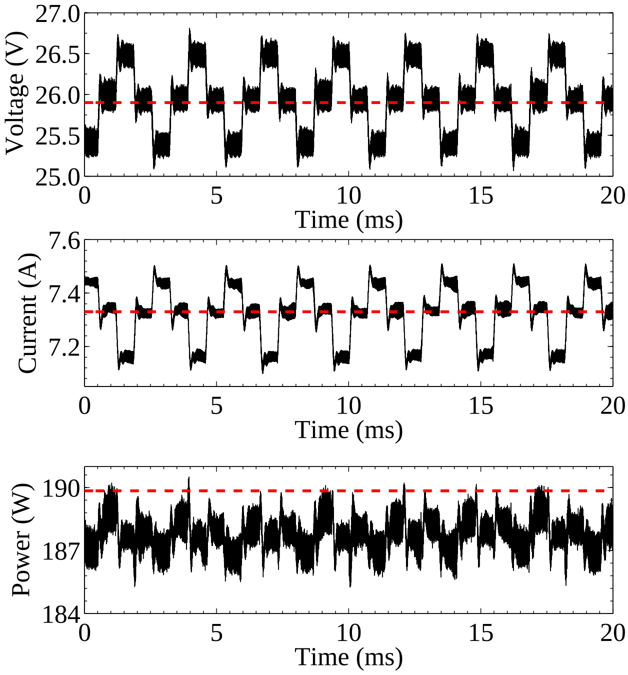

Figure 5.1: Measured input voltage, current and calculated power (black line) and their correspond MPP values (red dotted line) under 1000 W/m^2 irradiance with perturbation step $\Delta d = 0.0130$

The worst case condition occurs in low irradiance $G = 100\,\mathrm{W/m^2}$. The measured input voltage waveforms are presented in Appendix B (Fig. B.3), where the waveforms are plotted in different time intervals. It can be concluded that the voltage and power are settled down to their steady-state value before the next perturbation. However, MPPT operates under four operation points lowering the MPPT efficiency from the ideal three-point operation. This is due to the fact that the voltage changes at the ADC inputs are very small at low irradiance levels, where the MPP is actually the area of equal maximum power points. Therefore, noise can easily affect the power direction decision process. Nevertheless, the system is stable and MPPT is able to find the MPP.

The low irradiance measurement was also performed in Appendix B (Fig. B.2) by using the perturbation step $\Delta d = 0.006$, which was achieved by neglecting the quantization error of ADC. In this case, due to the quantization error and additional noise in the AD conversion, the power change cannot be measured accurately and the input voltage is drifting on both sides of the MPP thus reducing the energy yield.

5.3 Operation in Rapidly Changing Irradiance Conditions

The dynamic performance for MPPT algorithm was tested by using trapezoidal irradiance profile as defined in European standard. The most demanding condition for MPPT is the fastest irradiance slope, where the power variation is the highest. The standard defines irradiance slope 100 W/m^{2}s between irradiance levels 300 W/m^2 and

$1000\ \mathrm{W/m^2}$, which was used in measurement to guarantee the proper operation of the MPPT algorithm without drift.

To measure MPPT behavior in dynamic irradiance conditions, I-U curve parameters $(i_{\mathrm{sc}}, u_{\mathrm{oc}}, I_{\mathrm{mpp}}, U_{\mathrm{mpp}})$ were calculated based on the simulation model in different irradiance levels. Due to the fact that the minimum dwell time for each I-U curve is limited to 30 ms, 466 different I-U curves can be inserted to simulate whole the trapezoidal waveform with the rate of transition speed $\dot{G} = 100\,\mathrm{W/m^2s}$. Both the irradiance ramps were divided into 233 different I-U curves, where the correspond change between each point is $3\,\mathrm{W/m^2}$. From these parameters, the trapezoidal irradiance profile was generated to emulate the rapid irradiance variation.

The measurement started with constant $300\ \mathrm{W/m^2}$ irradiance level for 30 s, which ensures that MPPT has reached the initial condition. After the initial state was reached, the ramp profile was triggered via PC. The measured input voltage, current and calculated power over 28 s interval are shown in Fig. 5.2.

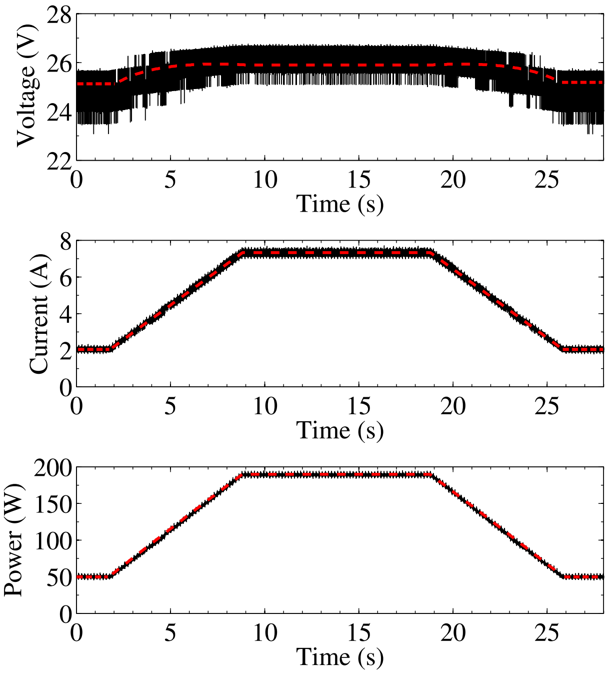

Figure 5.2: The measured PVG voltage, current and power (black line) and their corresponding MPP curve (red dotted line) under trapezoidal irradiance profile.

It can be noticed that the MPPT algorithm is able to track the MPP reasonable well. Since the perturbation step and sampling time were designed based on the fastest irradiance slope, the P&O algorithm is not diverged from the MPP in varying irradiance condition. However, the noise affects the power decision process of the MPPT and therefore, some energy is lost due to the non-optimum four-point operation. However, the dynamical efficiency for waveform shown in Fig. 5.2 yields 98.7 %, which is a little smaller than the maximum value of 99.8 %.

6. CONCLUSION

Despite a significant amount of developed MPPT algorithms, perturbative MPPT algorithms and their corresponding improved versions were analyzed more thoroughly in this thesis due to the fact that they have been shown to provide good balance between complexity and MPPT performance. However, the drawback of perturbative algorithms is the trade-off between steady-state oscillations and fast dynamics. Therefore, the design variables of the algorithm, the perturbation step size and the sampling period need to be optimized carefully to achieve highest possible efficiency and to ensure proper operation of the algorithm in all atmospheric conditions.

To achieve the fast dynamics in varying atmospheric conditions, sampling frequency of the perturbative algorithm should be selected as fast as possible. However, the sampling frequency should not be selected faster than the power settling time of a system, which can be obtained by analyzing the input voltage transient response of the system. Otherwise, the algorithm samples voltage and current too quickly yielding incorrect operation and reduced energy yield. The second design variable in perturbative MPPT algorithms is the perturbation step-size. It has a significant effect on MPPT performance in dynamic atmospheric conditions and steady-state efficiency. The steady-state efficiency can be approximated to be directly proportional to squared perturbation step and therefore, the amplitude needs to be kept as low as possible. However, the lower limit of the perturbation depends on external factors affecting the PVG output power such as irradiance variation, output voltage fluctuation and uncertainty factors in the measurement circuit.

In fact, the uncertainty factors such as high-frequency switching ripple and quantization error of AD converters play significant role in the proper operation of the perturbative algorithms. Therefore, the minimization of uncertainty must be focused on the noise sources that would influence most the decision process of the MPPT. Since all the uncertainty factors cannot be analyzed, it is recommended to select the largest perturbation step, which produces the required MPPT efficiency. It has been shown that when the perturbation step stays below 5 % of the MPP voltage value in STC, the maximum steady-state efficiency stays higher than 99 %. Then the sampling frequency needs to be designed so that the algorithm is not confused during fast-changing irradiance conditions.

In conclusion, high MPPT efficiency can be achieved with conventional perturbative algorithms if these are properly optimized. However, if the adequate performance is not attained with these MPPT techniques in spite of optimization, fixed-step perturbative algorithms can be further improved. One of the introduced improvements is to use an adaptive-step algorithm, which can overcome the steady-state oscillations in traditional perturbative methods. However, due the fact that the power prediction of these method are based also on two consecutive power samples, the simulations have been shown that robustness is poor in the most widely utilized adaptive-step algorithms in rapidly changing atmospheric conditions. The power prediction can be further improved by calculating one additional sample in the middle of the MPPT period, which ensures that drift phenomenon does not exist in fast-varying atmospheric conditions.

REFERENCES

[1] B. Bose, “Global warming: energy, environmental pollution, and the impact of power electronics,” *IEEE Ind. Electron. Magazine*, vol. 4, pp. 6–17, Mar. 2010.

[2] M. Villalva, J. Gazoli, and E. Filho, “Comprehensive approach to modeling and simulation of photovoltaic arrays,” *IEEE Trans. Power Electron.*, vol. 24, pp. 1198–1208, May 2009.

[3] H. Häberlin, *Photovoltaics: System Design and Practice.* Chichester, UK: John Wiley & Sons, Ltd, Feb. 2012.

[4] L. Nousiainen, J. Puukko, A. Mäki, T. Messo, J. Huusari, J. Jokipii, J. Viinamäki, D. T. Lobera, S. Valkealahti, and T. Suntio, “Photovoltaic generator as an input source for power electronic converters,” *IEEE Trans. Power Electron.*, vol. 28, pp. 3028–3038, June 2013.

[5] A. Mäki and S. Valkealahti, “Power losses in long string and parallel-connected short strings of series-connected silicon-based photovoltaic modules due to partial shading conditions,” *IEEE Trans. Energy Convers.*, vol. 27, pp. 173–183, Mar. 2012.

[6] J. Luoma, J. Kleissl, and K. Murray, “Optimal inverter sizing considering cloud enhancement,” *Solar Energy*, vol. 86, pp. 421–429, Jan. 2012.

[7] S. Valkealahti and K. Lappalainen, “Recognition of irradiance transitions caused by moving clouds harmful to the operation of pv systems,” in *29th European Photovoltaic Solar Energy Conf. and Exhibition*, pp. 2650–2653, 2014.

[8] S. Kjær, J. Pedersen, and F. Blaabjerg, “A review of single-phase grid-connected inverters for photovoltaic modules,” *IEEE Trans. Ind. Applications*, vol. 41, pp. 1292–1306, Sept. 2005.

[9] W. Xiao, N. Ozog, and W. G. Dunford, “Topology study of photovoltaic interface for maximum power point tracking,” *IEEE Trans. Ind. Electron.*, vol. 54, pp. 1696–1704, June 2007.

[10] T. Messo, J. Puukko, and T. Suntio, “Effect of mpp-tracking dc/dc converter on vsi-based photovoltaic inverter dynamics,” in *6th IET Int. Conf. Power Electron., Mach. and Drives*, PEMD. pp. 1–6, 2012.

[11] W. Xiao, W. Dunford, P. Palmer, and A. Capel, “Regulation of photovoltaic voltage,” *IEEE Trans. Ind. Electron.*, vol. 54, pp. 1365–1374, June 2007.

[12] R. Middlebrook, “Small-signal modeling of pulse-width modulated switched-mode power converters, in *Proc. of the IEEE*, pp. 343–354, 1988.

[13] R. Erickson and D. Maksimovic, *Fundamentals of Power Electronics.* Springer Science+Business Media, 2004.

[14] T. Messo, J. Jokipii, and T. Suntio, “Steady-state and dynamic properties of boost-power-stage converter in photovoltaic applications,” in *3rd IEEE Int. Symp. Power Electron. for Distributed Generation Syst.*, PEDG. pp. 34–40, 2012.

[15] J. Viinamäki, Design and implementation of a boost-power-stage converter for photovoltaic application. M.Sc. thesis, Dept. Elect. Eng., Tampere University of Technology, Tampere, 2013.

[16] G. Petrone, G. Spagnuolo, R. Teodorescu, M. Veerachary, and M. Vitelli, “Reliability issues in photovoltaic power processing systems,” *IEEE Trans. Ind. Electron.*, vol. 55, pp. 2569–2580, July 2008.

[17] T. Esram and P. Chapman, “Comparison of photovoltaic array maximum power point tracking techniques,” *IEEE Trans. Energy Convers.*, vol. 22, no. 2, pp. 439–449, 2007.

[18] B. Subudhi and R. Pradhan, “A comparative study on maximum power point tracking techniques for photovoltaic power systems,” *IEEE Trans. Sustainable Energy*, vol. 4, no. 1, pp. 89–98, 2013.

[19] S. Ji, D. Jang, S. Han, C. Roh, and S. Hong, “Analog control algorithm for maximum power tracker employed in photovoltaic applications,” in *IPEC*, pp. 99–103, 2010.

[20] N. Femia, G. Petrone, G. Spagnuolo, and M. Vitelli, *Power Electronics and Control Techniques for Maximum Energy Harvesting in Photovoltaic Systems.* CRC Press, 2012.

[21] X. Liu and L. Lopes, “An improved perturbation and observation maximum power point tracking algorithm for PV arrays,” in *35th Annu. Power Electron. Specialists Conf.*, pp. 2005–2010, 2003.

[22] A. N. A. Ali, M. H. Saied, M. Z. Mostafa, and T. M. Abdel- Moneim, “A survey of maximum mppt techniques of pv systems,” in *IEEE Energytech*, pp. 1–17, 2012.

[23] V. Salas, E. Olías, A. Barrado, and A. Lázaro, “Review of the maximum power point tracking algorithms for stand-alone photovoltaic systems,” *Solar Energy Materials and Solar Cells*, vol. 90, pp. 1555–1578, July 2006.

[24] K. Ishaque, Z. Salam, M. Amjad, and S. Mekhilef, “An improved particle swarm optimization (pso)-based mppt for pv with reduced steady-state oscillation,” *IEEE Trans. Power Electron.*, vol. 27, pp. 3627–3638, Aug. 2012.

[25] S. L. Brunton, C. W. Rowley, S. R. Kulkarni, and C. Clarkson, "Maximum power point tracking for photovoltaic optimization using ripple-based extremum seeking control," *IEEE Trans. Power Electron.*, vol. 25, pp. 2531–2540, Oct. 2010.

[26] T. Esram, J. Kimball, P. Krein, P. Chapman, and P. Midya, "Dynamic maximum power point tracking of photovoltaic arrays using ripple correlation control," *IEEE Trans. Power Electron.*, vol. 21, pp. 1282–1291, Sept. 2006.

[27] M. García, J. M. Maruri, L. Marroyo, E. Lorenzo, and M. Pérez, "Partial shadowing, mppt performance and inverter configurations: observations at tracking pv plants," *Progress in Photovoltaics: Research and Applications*, vol. 16, pp. 529–536, Sept. 2008.

[28] S. Kazmi, H. Goto, O. Ichinokura, and H. Guo, "An improved and very efficient mppt controller for pv systems subjected to rapidly varying atmospheric conditions and partial shading," in *Power Eng. Conf.*, AUPEC. pp. 1–6, 2009.

[29] R. Alonso, P. Ibáñez, V. Martínez, E. Román, and A. Sanz, "An innovative perturb , observe and check algorithm for partially shaded pv systems," in *13th European Conf. Power Electron. and Applications,* EPE, pp. 1–8, 2009.

[30] D. P. Hohm and M. E. Ropp, "Comparative study of maximum power point tracking algorithms," *Progress in Photovoltaics: Research and Applications*, vol. 11, pp. 47–62, Jan. 2003.

[31] K. Hussein, "Maximum photovoltaic power tracking: an algorithm for rapidly changing atmospheric conditions, in *IEE Proc. - Generation, Transmission and Distribution*, p. 59, 1995.

[32] D. Sera, L. Mathe, and T. Kerekes, "On the perturb-and-observe and incremental conductance mppt methods for pv systems," *IEEE Journal of Photovoltaics*, vol. 3, no. 3, pp. 1070–1078, 2013.

[33] T. Kim, H. Ahn, S. K. Park, and Y. Lee, "A novel maximum power point tracking control for photovoltaic power system under rapidly changing solar radiation," in *IEEE Int. Symp. Ind. Electron. Proc.*, ISIE, pp. 1011–1014, 2001.

[34] A. Zegaoui, M. Aillerie, P. Petit, J. Sawicki, A. Jaafar, C. Salame, and J. Charles, "Comparison of two common maximum power point trackers by simulating of pv generators," *Energy Procedia*, vol. 6, pp. 678–687, Jan. 2011.

[35] S. Kjær, "Evaluation of the "hill climbing" and the "incremental conductance" maximum power point trackers for photovoltaic power systems," *IEEE Trans. Energy Convers.*, vol. 27, pp. 922–929, Dec. 2012.

[36] N. Femia, G. Petrone, G. Spagnuolo, and M. Vitelli, "Optimization of perturb and observe maximum power point tracking method," *IEEE Trans. Power Electron.*, vol. 20, pp. 963–973, July 2005.

[37] H. Schmidt, B. Burger, U. Bussemas, and S. Elies, "How fast does an mpp tracker really need to be?," in *24th European Photovoltaic Solar Energy Conf.*, pp. 3273–3276, 2009.

[38] R. P. Venturini, V. Scarpa, G. Spiazzi, and S. Buso, "Analysis of limit cycle oscillations in maximum power point tracking algorithms," in *IEEE Power Electron. Specialists Conf.*, pp. 378–384, 2008.

[39] C. R. Sullivan, J. Awerbuch, and A. M. Latham, "Decrease in photovoltaic power output from ripple: simple general calculation and effect of partial shading," in *26th Annu. IEEE Applied Power Electron. Conf. and Exposition*, APEC, pp. 1954–1960, 2011.

[40] N. Femia, G. Petrone, G. Spagnuolo, and M. Vitelli, "A technique for improving p&o mppt performances of double-stage grid-connected photovoltaic systems," *IEEE Trans. Ind. Electron.*, vol. 56, pp. 4473–4482, Nov. 2009.

[41] H. Häberlin and P. Schaerf, "New procedure for measuring dynamic mpp-tracking efficiency at grid-connected pv inverters," in *24th EU PV Conf.*, pp. 21–25, 2009.

[42] B. Bletterie, R. Bruendlinger, and S. Spielauer, "Quantifying dynamic mppt performance under realistic conditions first test results - the way forward," in *21st Eur. Photovoltaic Solar Energy Conf. Exhibition*, pp. 2347–2351, 2006.

[43] F. Liu, S. Duan, F. Liu, B. Liu, and Y. Kang, "A variable step size inc mppt method for pv systems," *IEEE Trans. Ind. Electron.*, vol. 55, pp. 2622–2628, July 2008.

[44] A. Pandey, N. Dasgupta, and A. K. Mukerjee, "Design issues in implementing mppt for improved tracking and dynamic performance," in *32nd Annu. Conf. IEEE Ind. Electron.*, IECON, pp. 4387–4391, 2006.

[45] A. K. Abdelsalam, A. M. Massoud, S. Ahmed, and P. N. Enjeti, "High-performance adaptive perturb and observe mppt technique for photovoltaic-based microgrids," *IEEE Trans. Power Electron.*, vol. 26, pp. 1010–1021, Apr. 2011.

[46] A. Pandey, N. Dasgupta, and A. Mukerjee, "High-performance algorithms for drift avoidance and fast tracking in solar mppt system," *IEEE Trans. Energy Convers.*, vol. 23, pp. 681–689, June 2008.

[47] S. K. Kollimalla and M. K. Mishra, "Variable perturbation size adaptive p&o mppt algorithm for sudden changes in irradiance," *IEEE Trans. Sustainable Energy*, vol. 5, pp. 718–728, July 2014.

[48] A. Zbeeb, V. Devabhaktuni, and A. Sebak, "Improved photovoltaic mppt algorithm adapted for unstable atmospheric conditions and partial shading," in *Int. Conf. Clean Electrical Power*, pp. 320–323, 2009.

[49] D. Sera, R. Teodorescu, J. Hantschel, and M. Knoll, “Optimized maximum power point tracker for fast-changing environmental conditions,” *IEEE Trans. Ind. Electron.*, vol. 55, pp. 2629–2637, July 2008.

A. TABLES

Table A.1: Parameters for boost power-stage.

Parameter	Value
L	43 μH
C_1	20 μF
C_2	10 μF
r_{C1}	3 mΩ
r_{C2}	3 mΩ
r_{d}	45 mΩ
u_{d}	0.39 V
r_{sw}	6.2 mΩ

Table A.2: The maximum power point values in different irradiance levels, which are used in calculations.

Irradiance (W/m^2)	U_{mpp} (V)	I_{mpp} (A)	P_{mpp} (W)
50	21.51	0.27	5.88
100	23.37	0.64	14.90
200	24.65	1.38	29.17
300	25.22	2.13	53.60
500	25.73	3.62	93.09
1000	25.90	7.33	189.90

Table A.3: Calculated and simulated European efficiencies by using different perturbation step sizes.

Perturbation (% of $U_{\mathrm{mpp,stc}}$)	Calculated η_{eu} (%)	Simulated η_{eu} (%)
1	99.9	99.9
2	99.8	99.8
3	99.6	99.6
4	99.2	99.3
5	98.8	99.0
6	98.3	98.5
8	97.0	97.3
10	95.2	95.7

B. SIMULATION AND MEASUREMENT RESULTS

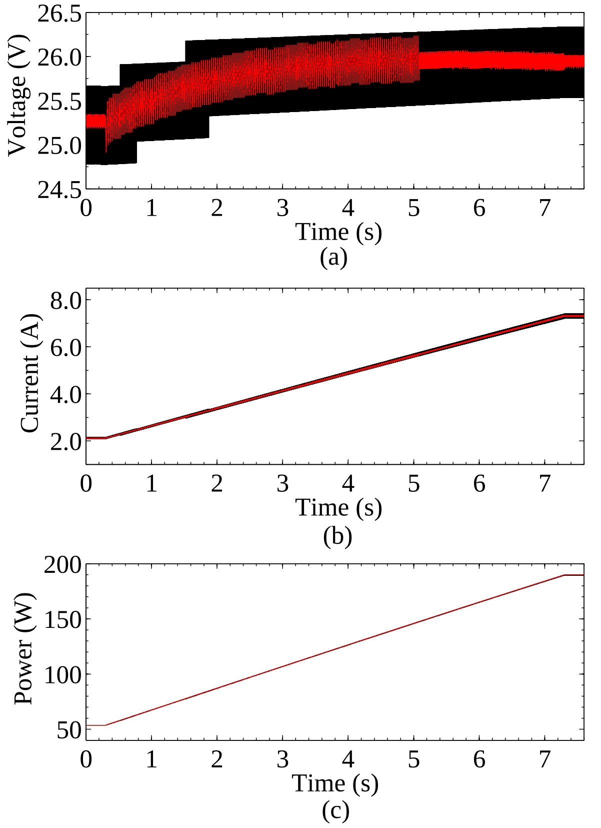

Figure B.1: Simulated PVG voltage (a), current (b) and power (c) waveforms under trapezoidal irradiance profile with perturbation step size $\Delta d = 0.006$ (black line) and $\Delta d = 0.00052$ (red line).

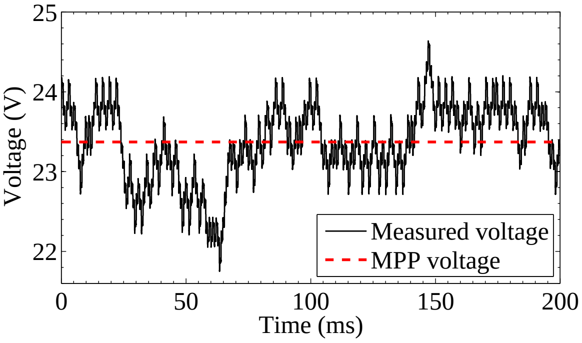

Figure B.2: Measured input voltage under $100\,\mathrm{W/m^2}$ irradiance with perturbation step $\Delta d = 0.006$.

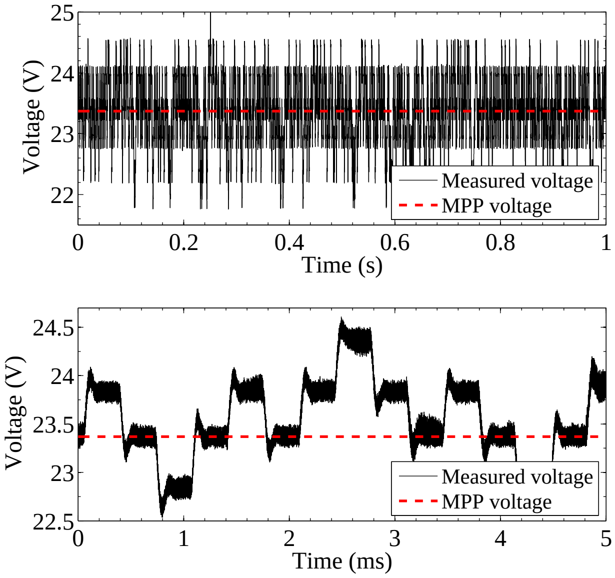

Figure B.3: Measured input voltage under constant 100 W/m^2 irradiance condition with perturbation step $\Delta d = 0.0130$.

C. MATLAB^{TM} SIMULINK MODELS OF THE MPPT ALGORITHMS

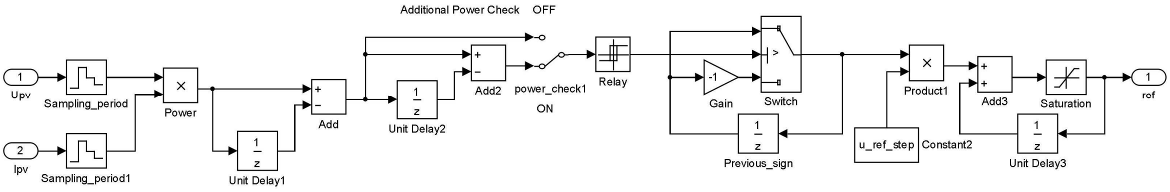

Figure C.1: Simulink model of fixed-step perturbative algorithm with the additional power check feature.

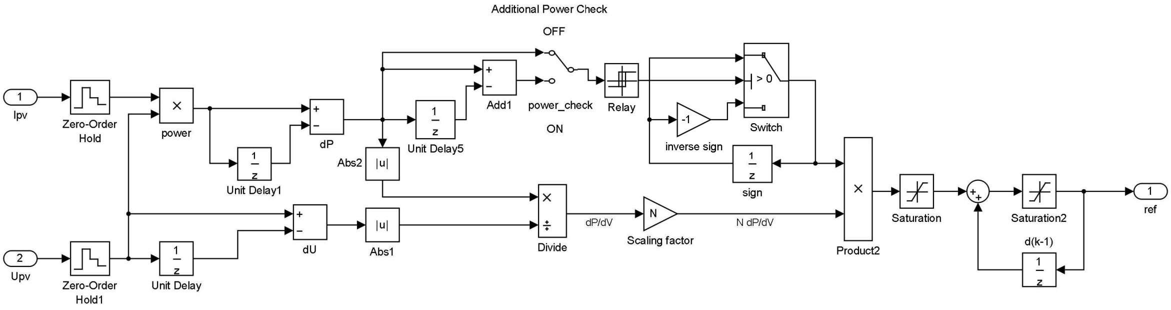

Figure C.2: Simulink model of adaptive-step perturbative algorithm with the additional power check feature.

D. SCHEMATICS OF CURRENT MEASUREMENT CIRCUIT

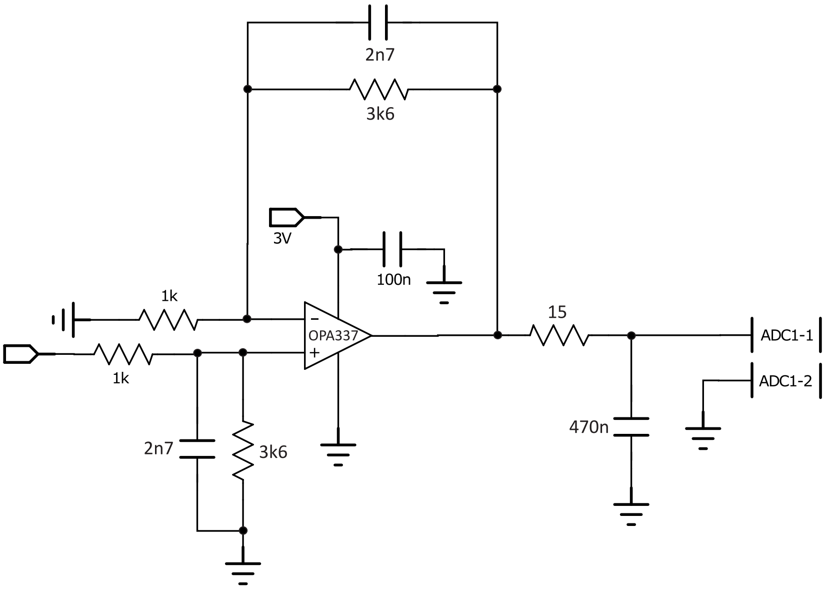

Figure D.1: Input current sensing measurement circuit.